Design and Development of a Modified Spouted Bed Coater for the Micro-encapsulation of Powders

A thesis presented in partial fulfilment of the requirements for the degree
of
Master of Technology
in
Chemical Technology

Massey University

New Zealand

Mr Peter Andrew Bishop

2003

Abstract

A modified spouted bed coater was designed and constructed for the micro-encapsulation of solid particles. The coating of small particles with a polymer film can alter physical factors such as taste and release rate. These properties are particularly important in the field of pharmacology as the nature of the coating can be changed to prolong or target drug release based on physiological conditions such as pH and time.

The spouted bed coater was modified to induce gas and particle recirculation through a draft tube containing a venturi to increase droplet and particle mixing, while a high velocity gas jet and large diameter draft tube promotes the recirculation of gas and solid within the apparatus. The effectiveness of the design was tested in terms of gas and solid mass flows through the draft tube using a venturi within the draft tube and an induction detector to measure the mass flow.

To determine the effectiveness of the coater design in terms of coalescence and the influence of operational variables, a factorial experiment was conducted. The result of this experiment showed that the coalescence of particles was dominated by the relative humidity in the apparatus which was unable to be directly related to the operational variables.

The capacity to micro-encapsulate particles was demonstrated by coating fine table salt with an acrylic polymer Eudragit NE 40D in combination with bentonite clay as a free flow agent or glident. The results of this trial showed the distribution of polymer/clay and the reduction in dissolution rate as a function of particle size.

Acknowledgments

I would like to thank, my supervisor, Dr Jim Jones for the valuable guidance in the area of writing and for the opportunity to work on an exciting and challenging project. The technical staff in particulary, Russell Watson, Bruce Collins and John Edwards for there assistance in turning sketches into hardware. I would like to thank my wife, Janey and children, Claramae, Vanessa, Andrew and Caroline, for their support through the difficult times and the joy they bring to every day. My Thanks go also to my mother, Anne, and father, Derrick, for their encouragement over the years, with my struggle with dyslexia. The late Dr Jean Seabrook and SPELD for helping me find my potential.

Table of Contents

Nomenclature

a	particle radius, m
A	area of droplet, m^2
A_a	area of atomizer air nozzle, m^2
A_t	total area of atomizer air nozzle orifice, m^2
c	rupture energy constant
C_o	capillary pressure of touching spheres, Pa
C_D	coefficient of drag
d_p	particle diameter, m
$d_{p(max)}$	maximum particle diameter for coalescence, m
D_d	diameter of droplet, m
D_{dt}	diameter of draft tube, m
$D_{j(0)}$	diameter of inlet gas jet at z = 0, inlet gas nozzle diameter, m
D_{50}	50% of the mass of particles are less than this diameter, m
D_{90}	90% of the mass of particles are less than this diameter, m
D_{max}	maximum diameter of draft tube, m
dM/dt	rate of mass change, kg/s
e	coefficient of restitution
F_γ	surface tension force, N
F_{sp}	capillary suction force, N
F_{total}	total liquid bridge force, $F_\gamma+F_{sp}$, N
G	granule or particle growth rate , m/s
g	gravitational constant, m/s^2
h	half the separation distance between particle surfaces, m
h_c	convection heat transfer coefficient, $W\ m^{-2}\ K^{-1}$
h_0	initial height of liquid layer on particle surface, m
h_a	height of surface asperity on surface of core particle, m
H	height, m
H_{min}	minimum height of draft tube, m
k_d	thermal conductivity of droplet, W/mK
K_f	coefficient of resistance of fabric, kPa s/m
K_p	coefficient of resistance of powder, kPa m s/kg

M_p individual particle mass, kg

M_s total mass of solids in apparatus, kg

M_{sf} mass of solids on filter fabric, kg

m mass of particle, kg

N number concentration, particles/m^3

N_{pixel} number of pixels

P pressure, Pa

Q_a mass of atomizer air flow, kg/s

Q_l mass of atomizer liquid flow, kg/s

Q_g mass flow of gas, kg/s

$Q_{g(Z)}$ mass flow of gas at point z on the z axis, kg/s

Q_s mass flow of solids, kg/s

Q_b mass flow of binder, kg/s

r_1 minimum radius of liquid bridge, m

r_2 radius of curvature of liquid bridge, m

t time, s

$t_{circ.}$ circulation time, s

t_r gas retention time, s

u velocity of particle, m/s

u_0 initial particle velocity, m/s

$u_{0(max)}$ initial maximum particle collision velocity for coalescence, m/s

U velocity of gas, m/s

U_t settling velocity of particle, m/s

v_r radial particle velocity, m/s

V_d volume of atomized droplet

v_{rel} relative velocity, m/s

V_p volume of particle, m^3

V_b volume of liquid bond, m^3

v velocity, m/s

W work, J

x particle separation distance, m

Z distance from jet, m

Dimensionless Groups

b^*	binder to solids volume ratio, V_b/V_p
b^*_c	critical binder to solids ratio, $(1+h_a/a)^3-1$
C_a	Capillary number, $\mu u/\gamma$
Nu	Nusselt number, $h_c D_d / k_d$
Re	Reynolds number, $U_g D \rho_g/\mu_g$
St_v	Stoke's number, $2mu_o/3\pi\mu a^2$
V_b^*	dimensionless bridge volume, V_b/a^3
W^*	dimensionless bond rupture energy, $W/\gamma a^2$
ε	dimensionless particle separation distance, 2h /a

Greek

α	contact angle, degrees
β	half-filling angle, degrees
ΔH_{vap}	latent heat of vaporization, J/kg
ΔT_{lm}	log mean temperature difference, K
μ	viscosity, kg/ms
ρ	density, kg/m^3
ρ_s	density of solid, kg/m^3
γ	surface tension, N/m
ε_z	voidage of fluid bed at point z on the z axis
θ	gas jet dispersion angle, degrees
φ	the binder liquid contact angle
ω	powder loading, kg/m^2

1 Literature Review

Granulation and micro-encapsulation are important processes in the production of a wide range of specialty products such as pressure sensitive adhesives, carbonless copy ink and controlled release fragrances and pharmaceuticals [Finch,1993]. Granulation is the process of particle size enlargement, which may occur via the coalescence of smaller particles, or the progressive coating of a particle with a layer which hardens to increase the particle size. Micro-encapsulation is the process of coating the surface of small particles, with a diameter less than 1 mm, with an film which alters the chemical or physical properties of the particle.

The goal of this project is to develop a device that will in a single unit operation granulate and micro-encapsulate powders. For ease of description this device is called the modified spouted bed. To obtain the required design parameters for the construction of this apparatus the literature review concentrates on three main areas:

1. Current practices in micro-encapsulation
2. Granulation mechanisms
3. Micro-encapsulation agents.

1.1 Current Practices in Micro-encapsulation

Liquid suspension micro-encapsulation

The first method of micro-encapsulation was developed by Bungenberg de Jong and Kruyt in 1930 [Finch, 1993]. They developed a liquid phase separation process termed "coacervation". In this process the core particles (solid or liquid) are suspended in a solution of the coating polymer. The polymer is then induced to separate from the solution as a viscous liquid phase which encapsulates the suspended core particles. The polymer is then solidified by cooling or by further polymerization by the addition of a catalyst or cross linking agent. The resulting encapsulated solid is then removed by filtration.

Other liquid suspension methods that have been developed are [Finch, 1993]:

1. Interfacial polymerization
2. Solvent evaporation from emulsion, including spray drying
3. Gelation in the liquid state.

These four methods form the mainstay of micro-encapsulation and are widely used in the production of pressure sensitive adhesives, carbon-less copy ink, controlled release fragrances, pharmaceuticals, and in taste masking. While these techniques are widely used, they require complex chemical and physical operating conditions and in most cases require three process stages; suspension and encapsulation, separation and finally drying.

Gas suspension methods

The gas suspension techniques can be divided into aerosol and fluid bed methods. Robbins *et al.*[1963] list the following aerosol micro-encapsulation methods:

1. Condensation of a coating agent on nuclei core particles in the aerosol phase
2. Spray drying of a two-phase suspension or emulsion
3. High turbulence mixing of aerosol particles with a liquid coating agent by using a twin fluid type atomizer
4. Opposite electrolytic charging of solid and liquid particles followed by their combination in the aerosol phase
5. Condensation and polymerization of an organic monomer from the gas phase onto aerosol particles.

The most effective of these methods reported by Robbins *et al.*[1963] was the condensation and polymerisation of isoprene on droplets of phosphoric acid. The droplets of phosphoric acid were produced using a twin fluid jet atomizer and passed co-currently with a gas mixture containing isoprene vapour and a catalyst nitrogen dioxide through a short u-tube chamber to allow condensation and polymerization to occur on the droplet surface. The coated product was then recovered by allowing the droplets to settle in the bottom of the u-tube. The encapsulation efficiency was determined by the titration of a weighed quantity of product particles with sodium hydroxide solution to assess the free residual phosphoric acid level. The results showed that 92 % of the phosphoric acid was encapsulated. This work was funded by the US Army Chemical Centre and is largely unpublished as the objective of Robbins's [1965] patent US03219476 was the encapsulation of chemical warfare agents.

The disadvantage of this process is that the concentration of particles in the gas suspension must be low, in the order of 1-3 mg/l [Robins *et al.* 1963], thus making product recovery difficult due to the volume of gas to be handled.

Fluid bed processes

The Würster process is one of the most commonly used fluidized bed systems for micro-encapsulation, patented by Würster *and Lindlof*, [1965], (fig.1.1). In this process the fluidized bed is partitioned into two horizontal zones by a tubular insert or draft tube, which extends from above the particle bed height to just above the base plate of the bed.

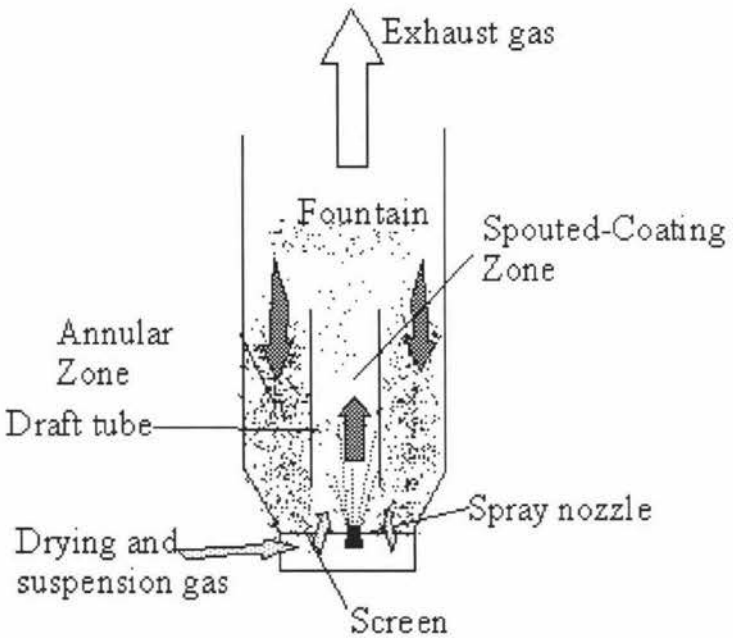

Figure 1.1 Apparatus of Würster and Lindlof [1965].

The clearance from the base plate allows particles from the fluidized annular zone to enter the spouted-coating zone. In the spouted-coating zone the particles are transported pneumatically upwards and out of the draft tube as liquid is applied co-currently to the particles from a spray nozzle positioned in the base plate of the fluid bed. On leaving the draft tube the gas stream slows and the particles dis-entrain from the gas stream and

return to the annular zone under the influence of gravity. The successful operation of this process relies on the coating drying or hardening prior to the particles returning to the annular zone where agglomeration can occur between wetted particles.

Partitioning of the annular and spouted zones reduces the effect of over-fluidization of the annular zone and allows coherent spouting of fine particles, which is not possible in a normal spouted bed due to the physical parameters which control the spouting phenomena [Mathur and Epstein, 1974]. In a normal spouted bed without a draft tube, the loss of coherent spouting occurs as a function of bed height, superficial gas velocity entering the spout, particle diameter, and gas inlet diameter. As the height of the bed increases, more gas diffuses across the spouted zone interface into the annular zone. This lowers the superficial gas velocity at the top of the spout until there is insufficient gas flow in the spout to penetrate the upper surface of the bed. The spouted bed then collapses to form a static bed. Increasing the gas velocity in the spout also results in the loss of spouting as the two zones collapse to form a bubbling or slugging bed.

In addition to bed height and maximum gas velocity, the formation of a coherent spouted bed is also affected by the particle size of the material in the bed. A reduction in particle size reduces the operational range of gas velocities [Mathur and Epstein, 1974]. For sand 0.42-0.83 mm in diameter, the operational range of gas velocity is 0.15-0.2 m/sec, while for semicoke of 1-5 mm the range is 0.4 -1.2 m/s. The size of the particles also restricts the diameter of the gas inlet nozzle, which must be less than 20 particle diameters in diameter to prevent choking [Wang *et al.*, 2000].

Dannelly and Leonard [1976] introduced a large cone shaped partition and an aerofoil below the screen in the gas inlet to increase drying and spray mixing time in their

apparatus. This also reduced the abrasion of particles in the annular zone, which is no longer fluidized and is under a slight suction due to the venturi effect produced by the inserts, as shown in fig.1.2.

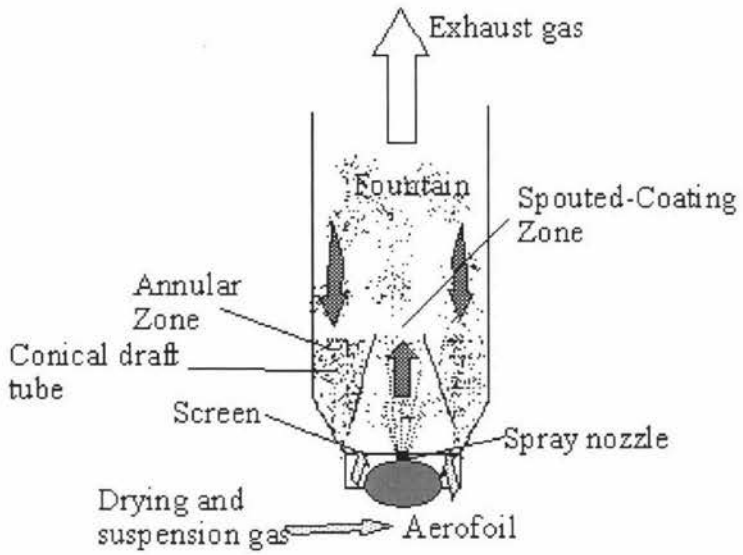

Figure 1.2 Apparatus of Dannelly & Leonard [1976].

The use of a venturi to re-circulate gas and particles has also been introduced by Larson and Mallak [1963] to reduce the total gas flow requirements of the coating process, as shown in fig.1.3.

The most turbulent gas suspension method, used for micro-encapsulation of particles less than 20 microns, is the "Fluid Energy Mill"[Smith-Johannsen and Wendell., 1976], as shown in fig.1.4. In this system, a mixture of finely ground polymer and core materials are jointly injected into a venturi by a high velocity gas jet, which accelerates the particles to supersonic velocities. This high velocity aerosol enters a circulating ring in which the gas temperature melts the polymer. The circulating particles and droplets of polymer undergo multiple collisions, which evenly distributes the polymer over all the particles. The particles less than 20 microns escape the

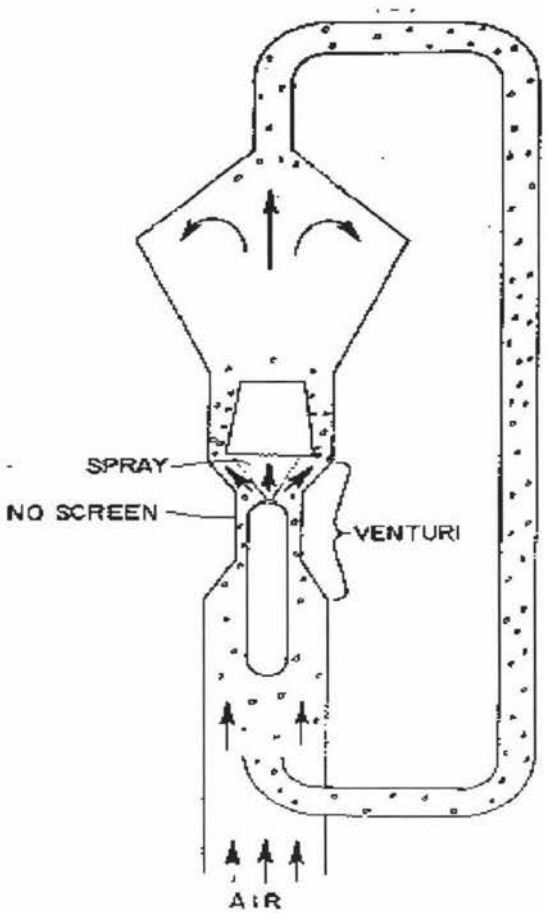

Figure 1.3 Apparatus of Larson and Mallak [1963], [US patent 3,110,626].

circulation system via an internal vent positioned on the inner surface of a curved bend which, due to centrifugal forces, prevents particles greater than 20 microns leaving the circulation loop. The larger particles then circulate until attrition reduces their size to less than 20 microns.

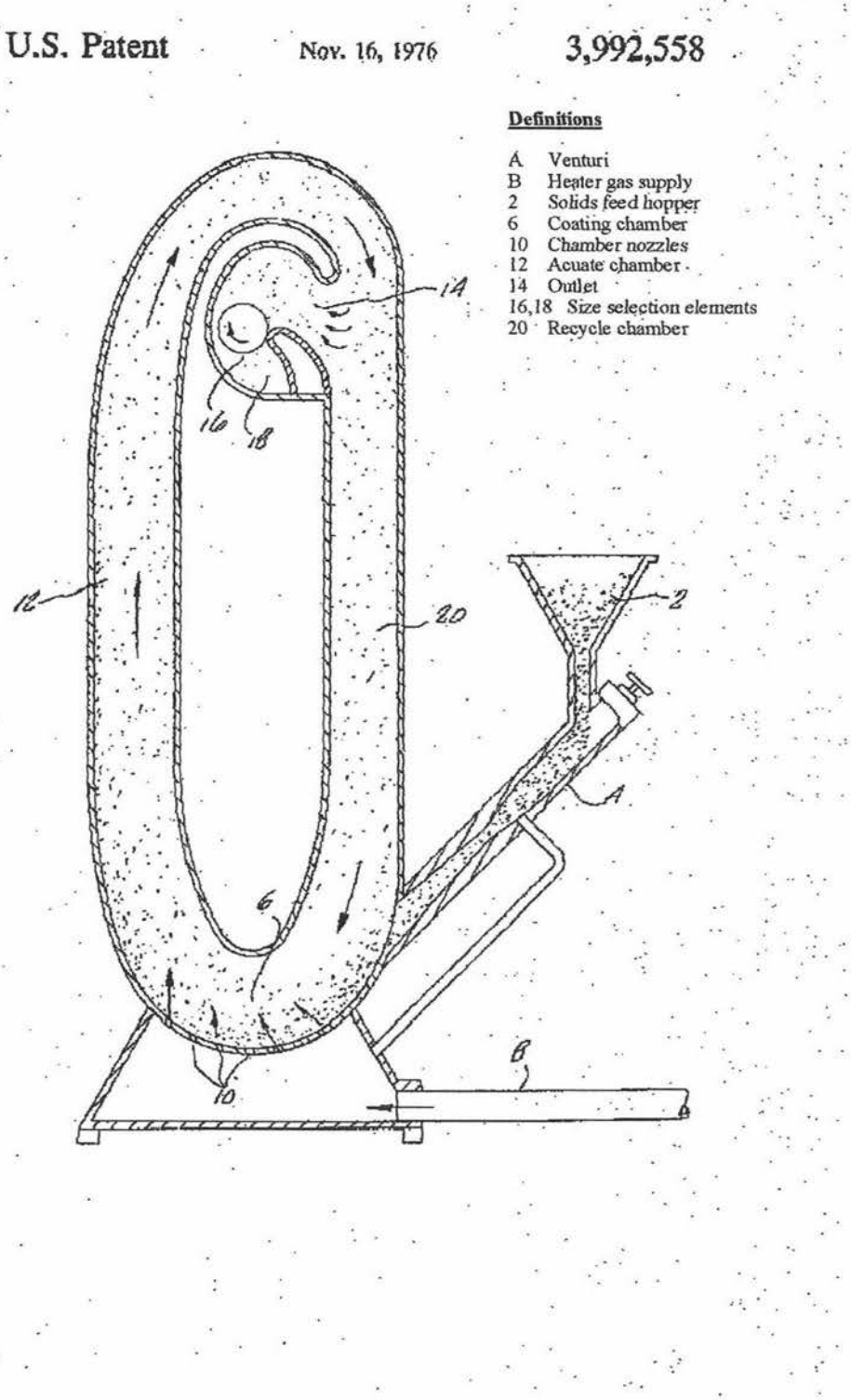

Figure 1.4 Fluid energy mill [Smith-Johannsen and Wendell, 1976. US patent 3992558]

1.2 Granulation and Encapsulation Mechanisms

Determining the conditions under which coalescence occurs is critical for the successful design of the micro-encapsulation or granulation system. Ennis *et al.* [1991] and Simons *et al.*[1994] discuss the collision energy and potential bond energy of a mobile liquid bridge between two particles as being the criteria that determine whether or not colliding particles will coalesce. Both authors present sound arguments based on different treatments of the problem. Ennis *et al.* uses a viscous force model, while Simons *et al.* use a capillary force model, to estimate the bond energy. This leads to different solutions which challenge each other in terms of the importance of binder viscosity and surface tension. For a given system both workers calculate the maximum particle size that can coalesce by considering the kinetic energy of the collision and the loss of energy due to bond formation.

Viscous dissipation model

Ennis *et al.* [1991] proposed that the likelihood of a collision between two wet particles, resulting in coalescence, is predominantly governed by the loss of kinetic energy due to viscous dissipation, which occurs as a result of the movement of liquid layers on the surfaces of the particles during the collision. The viscous dissipation criteria for coalescence is derived based on the following conditions. Consider two granules of radius a, approaching each other with a relative velocity $2u_0$, where u_0 is the initial individual particle velocity, and covered by an initial layer of binder thickness h_0. The minimum velocity required for a granule to rebound is obtained from the force balance eqn. 1.1, as derived by Ennis *et al.*[1991].

$$m\frac{du}{dt}=\pi\gamma a[\sin^2\varphi(C_0+2)+\frac{3}{2}\frac{C_a}{\varepsilon}+O(C_a\ln\varepsilon)] \qquad \textbf{(1.1)}$$

The left hand side of eqn.1.1 expresses the collision force of the granule, which is the mass of the granule m multiplied by the deceleration du/dt. The right-hand side of the equation contains the capillary and viscous force components. The capillary suction is defined as $\pi\gamma a\sin^2\varphi(C_0+2)$, where γ is the surface tension, φ is the contact angle of the liquid bridge, which defines the surface area covered by the liquid bridge, and C_0 is the dimensionless Laplace-Young pressure difference which acts over the granule surface covered by the liquid bridge. The viscous force is represented by $\pi\gamma a3C_a/2\varepsilon$, where $\varepsilon = 2h_0/a$, is the initial dimensionless particle separation, C_a is the capillary number $C_a = \mu u/\gamma$, which is the ration of viscous force over the surface tension force, μ is the binder viscosity, u is the instantaneous collision velocity and γ is the binder surface tension. The fourth term $O(C_a \ln\varepsilon)$ is not clearly described by Ennis *et al.*, but appears to be related to the viscous lubrication pressure.

Equation 1.1 in its present form has no analytical solution, however Ennis *et* al. [1991] simplified this equation by ignoring the capillary suction contributions and retaining only the dominant viscous contributions. The capillary suction effect is negligible as the energy of bond formation of the liquid bridge due to the capillary suction is equal to the bond rupture energy. The viscous dissipation force dominates eqn.1.1, as the particles approach each other, ε tends to 0, which results in the viscosity force term, $3C_a/2\varepsilon$ tending to ∞ and the third term tends to 0. Thus only the viscous dissipation, term 2 in eqn 1.1 needs to be retained. The substitution of dx/dt for u and x the dimensional particle separation $x = 2h$, simplifies eqn 1.1 to eqn 1.2, as given by Ennis *et al.*[1991].

$$m\frac{du}{dt} = \frac{3}{2}\pi\mu a^2\frac{dx}{dt}\times\frac{1}{x} \qquad \textbf{(1.2)}$$

The solution of eqn 1.2 was obtained by Ennis *et al.*[1991] for the movement of two approaching particles from $x = h_0$ to $x = 2h$, where the particles initially have an approach velocity of u_0.

$$u = u_0[1 - \frac{1}{St_v}\ln(\frac{h_0}{x})] \qquad \textbf{(1.3)}$$

were St_v is the Stokes number, which is the ratio of kinetic collision force and the viscous dissipation force, $St_v = 2mu_0/3\pi\mu a^2$. This solution allows the velocity of a colliding granule to be calculated as a function of the Stokes number for the collision and proportional distance travelled through the binder layer ($2h/x$).

Ennis *et al.*[1991], determines the critical value of the Stokes number which gives the limit of granule coalescence. This was derived by assuming the collision may only reach a separation of h_a, the asperity height due to the surface roughness, and that the granule rebounds with a velocity equal to the particle collision velocity multiplied by the coefficient of restitution e, which accounts for the non-elasticity of the solid rebound. The critical Stokes number is then obtained so that the granule velocity u = 0 at distance $x = h_a$, this result is given as eqn 1.4.

$$St_v^* = (1 + \frac{1}{e})\ln(\frac{h_0}{h_a}) \qquad \textbf{(1.4)}$$

Equating the Stokes number, St_v, with the critical Stokes number, St_v^*, yields either the maximum granule diameter for coalescence , $d_{p(max)} = 2a$, given the initial collision velocity or the maximum initial collision velocity, $u_{0(max)}$, given the particle size. Assuming spherical granules with a known asperity height, the relationships reduce to equations 1.5 and 1.6.

$$d_{p(\max)} = \frac{9\mu(1+\frac{1}{e})\ln(\frac{h_0}{h_a})}{4u_0\rho_s} \qquad (1.5)$$

$$u_{0(\max)} = \frac{9\mu(1+\frac{1}{e})\ln(\frac{h_0}{h_a})}{4a\rho_s} \qquad (1.6)$$

Capillary suction models

A more traditional model of wetted particle bonding is the capillary suction model initially developed by Rumpf [1962] and further by Simons *et al.*[1994]. In this model only the capillary force on the liquid bridge are considered. These forces are described by the surface tension force F_γ due to the reduction in surface area of the liquid exposed to the air and the suction force F_{sp} due to the pressure difference created by the curvature of liquid surface of the liquid bridge. These forces are assumed to act over the minimum radius of the bond r_1 as shown in figure 1.5

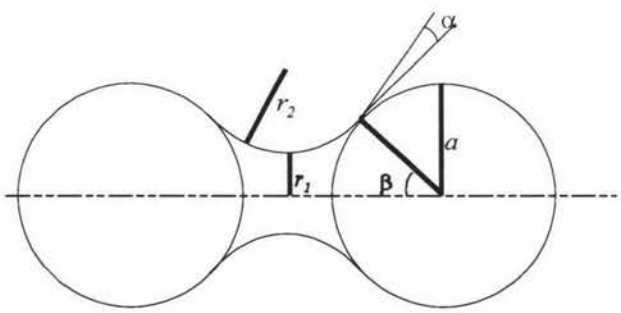

Figure 1.5 Geometry of liquid bridge bonding two equal size spheres.

Given these approximation that the two forces are quantified as:

$$F_{\gamma}=2\pi r_1\gamma \tag{1.7}$$

$$F_{sp}=\pi r_1^2\Delta P \tag{1.8}$$

where the pressure difference relates to the Young-Laplace eqn 1.9.

$$\Delta P=\gamma\left(\frac{1}{r_2}-\frac{1}{r_1}\right) \tag{1.9}$$

If the contact angle α is assumed to be zero degrees, r_1 and r_2 can be represented by the eqn 1.10 and 1.11 when the spheres are touching .

$$r_2=a(\sec\beta-1) \tag{1.10}$$
$$r_1=a(1+\tan\beta-\sec\beta) \tag{1.11}$$

By combining F_{γ} and F_{sp} an expression for the total capillary force in the bond can be obtained.

$$F_{Total}=\frac{2\pi r_2\gamma}{1+\tan\frac{\beta}{2}} \tag{1.12}$$

Based on this expression of force, Simons *et al.*[1994] developed a dimensionless expression for the bond rupture energy, W^*, by assuming β is independent of the particle separation. Simons *et al.* then integrated the force over the particle separation from zero

to the bond rupture point. The bond rupture point has been shown by Lian *et al.*[1993] to be proportional to the cube root of the bond volume, $V_b^{1/3}$ and the contact angle, α in radians, as defined by the critical separation distance, $S_c = (1+0.5\alpha)V_b^{1/3}$; thus at $\alpha = 0$, the critical separation distance equals $V_b^{1/3}$. From this the expression for the dimensionless bond energy was derived by Simons *et al.*as eqn 1.13 and 1.14 .

$$W^* = \frac{W}{\gamma a^2} = cV_b^{*0.5} \qquad \textbf{(1.13)}$$

$$\textit{where} \qquad V_b^* = \frac{V_b}{a^3} \qquad \textbf{(1.14)}$$

W is the rupture energy of the pendular bond, γ is the surface tension of the binder/air interface, a is the particle radius, V_b is the liquid bridge volume, V^*_b is dimensionless bridge volume and c which is the rupture energy constant which appears to result from the integrational constant, related to $(1+0.5\alpha)$. Simons *et al.* given c as 1.8 for a one particle half bond or 3.6 for the full bond.

Conversion of Simons et al.[1994] model to give maximum collision velocity

To compare the models of Simons *et al.*[1994] and Ennis *et al.*[1991] the two models must be manipulated into formats which reveal the maximum collision energy which two wetted particles may have prior to bond rupture or rebound. This is achieved by applying the collision energy and bond energy balance to the model of Simons *et al.* resulting in expressions for the maximum initial collision velocity, $u_{0(max)}$, for particle coalescence. This conversion requires the substitution of eqn. 1.14 into eqn. 1.13 giving eqn. 1.15.

$$W^* = \frac{W}{\gamma a^2} = c\left(\frac{V_b}{a^3}\right)^{1/2} \qquad \textbf{(1.15)}$$

Rearranging this, the bond rupture energy, W, is obtained as a function of the particle radius, a, the surface tension γ, and the bond volume, V_b.

$$W = c\gamma(aV_b)^{1/2} \tag{1.16}$$

The collision energy, E_k, can be equated to the bond rupture energy, W, where m is the particle mass.

$$E_k = \frac{1}{2}mu_{0(\max)}^2 = c\gamma(aV_b)^{1/2} \tag{1.17}$$

Equation 1.17 can then be rearranged to give $u_{0(max)}$, the maximum collision velocity, eqn. 1.18.

$$u_{0(\max)} = \left(\frac{2c\gamma}{m}\right)^{1/2}(aV_b)^{1/4} \tag{1.18}$$

As m is a function of the particle volume, V_p, and density, ρ_s , $V_p\,\rho_s$ can be substituted for m, resulting in eqn. 1.19.

$$u_{0(\max)} = \left(\frac{2c\gamma}{\rho_s V_p}\right)^{1/2}(aV_b)^{1/4} \tag{1.19}$$

Assuming spherical particles $V_p = 4\pi a^3/3$ 1.19 gives the equation 1.20 relating the maximum collision velocity and particle radii under which coalescence of two colliding particles is viable.

$$u_{0(\max)} = \sqrt{\frac{3c\gamma}{2\rho_s\pi}} \times V_b^{1/4} \times a^{-5/4} \tag{1.20}$$

V_b can be expressed in terms of V_p by introducing the binder to particle volume ratio b^*, thus $V_b = b^* V_p = 4b^* \pi a^3/3$ .This substitution results in equation 1.21, which is more practical as b^* is commonly used to describe granulation rates.

$$u_{0(\max)} = \sqrt{\frac{c\gamma}{\rho_s a}} \times \sqrt[4]{\frac{3b^*}{\pi}} \qquad \textbf{(1.21)}$$

Comparison of viscous dissipation and capillary suction models

Both the viscous dissipation and capillary suction models result in expressions for the maximum collision velocity which particles may have before coalescence becomes unfavourable. The models are distinct as the viscous dissipation model considers the dynamics of the collision involving the viscous layer and is dominated by the liquid viscosity, while the capillary suction/bond rupture energy model considers the stability of the liquid bridge in the post collision state, where the bond force is dominated by the surface tension of the binder.

A maximum collision velocity can be defined for the two models which result in coalescence. The bond rupture model requires the assumption of perfectly elastic particles without any viscous dissipation; thus, the kinetic energy of collision is equated to the energy required to rupture the liquid bridge. The viscous dissipation model calculates the maximum collision velocity before rebound occurs. The maximum collision velocities for the two models can be compared as a function of particle size for three binder liquids, water, paraffin and a water solution containing 30% polyethylene glycol 6000. For this comparison the following variables are fixed $b^* = 0.13$, $\rho_s = 2500$ kg/m^3, $h_a = 0.5$ μm, $e = 1$. The height of the liquid layer h_o can be approximated, based on the increase in radius due to a uniform layer of binder over the surface of a spherical particle.

Thus for a particle volume, V_p, which is coated by binder equal to $b*V_p$, the volume of the particle increases to, $V_p + b*V_p$ and thus the wetted particle radius increases to equal, $a(1+b*)^{1/3}$ and so the difference in particle radius is given by equation 1.22.

$$h_0 = a((1+b^*)^{1/3} - 1) \qquad \textbf{(1.22)}$$

Table 1.1 Physical properties of binders

Binder Liquid	**Viscosity Nsm^{-2}**	**Surface Tension Nm^{-1}**
Water[a]	0.001	0.072
Paraffin oil[a]	1	0.026
30% PEG(measured)	0.031	0.06

[a] - Oliver & Boyd Science Data Book 1986
Measured- viscosity using Brookfield viscometer
Surface tension using Du Nuoy Tensiometer

The results, Fig 1.6, shows that the capillary suction model gives little response to the changes in binder type as the maximum collision velocity is proportional to the square root of the surface tension and the negative square root of the particle radius. The capillary suction model also shows no response to the binder layer thickness, which in this example falls below the surface asperity when the particle diameter is less than 24 microns.

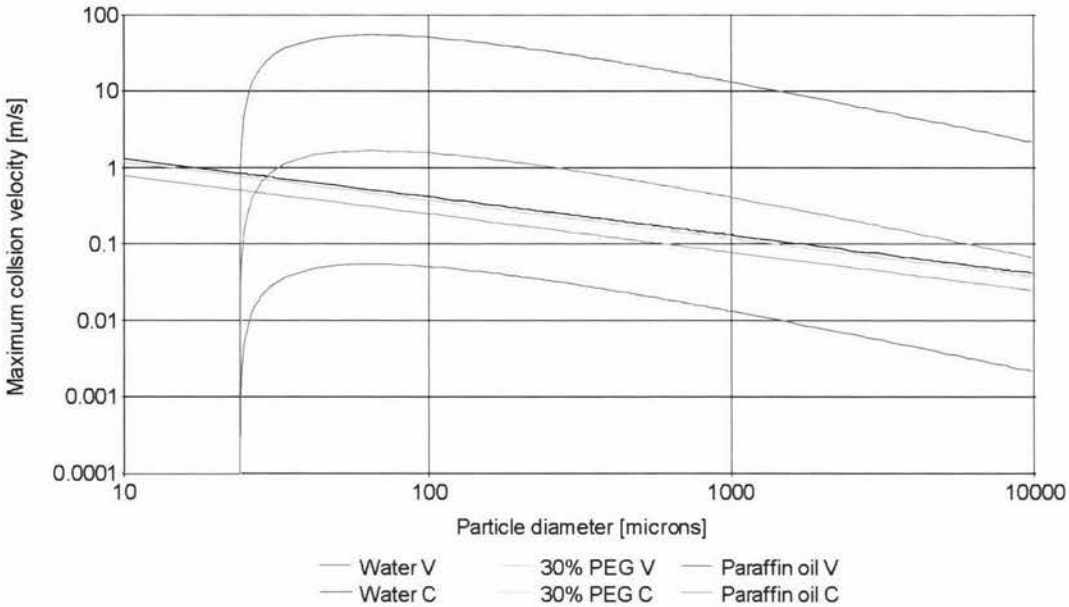

Figure 1.6 Effects of binder, viscosity and surface tension on the maximum collision velocity for particle coalescence for the viscous dissipation (V) and the capillary suction (C) models.

In sharp contrast, to the capillary suction model, the viscous dissipation model shows a larger response to binder type with the maximum collision velocity being proportional to the binder viscosity and inversely proportional to the particle radius.

The viscous dissipation model also shows a realistic response to the effective liquid film thickness, which is zero when the particle diameter is 24 micron, due to (h_0/h_a) being equal 1 which makes coalescence not possible. Following from this result the minimum liquid layer for particle coalescence occurs when $h_0 = h_a$, substituting this equality and rearranging eqn.1.22, the critical binder to solids volume ratio for coalescence may be estimated using equation 1.23.

$$b_c^* = (1+\frac{h_a}{a})^3 - 1 \qquad \textbf{(1.23)}$$

Based on the resulting equations for maximum collision velocities the two models can be applied to the following situations: the capillary suction model dominates systems of coalescence where low viscosity binders are used such as water, and the viscous dissipation model dominates systems with moderate viscosities such as 30% PEG and Paraffin oil. However, both models are dependent on availability of surface liquid and thus without the binder to solids ratio being greater than the critical binder ratio, b_c^*, agglomeration is not possible.

1.3 Encapsulation Agents

A wide range of coating agents are currently in use. Finch [1993] lists 28 natural polymers and 27 synthetic polymers, each of which have different physical and chemical properties. For application in this work, the coating agent must have the following characteristics:

- Non-toxic
- Hardens on drying to form an impermeable film
- Forms an aqueous solution or dispersion at room temperature 10-35 ^{0}C.

These restrictions then reduce the possibilities to:

- Protein-Aldos polymers: protein (insulin) and oxidized dextran [Li, 1998], protein (lactases) and glutaraldehyde [Zhou and Chen, 2000].
- Cross linked gelatin-gum arabic or gelatin- carboxy methyl cellulose
- Latex

Latex coatings

Of these options the latexes are commonly used in fluid bed applications [Finch, 1993] and so will be used in the remainder of this study. Latex is a generic term for an aqueous dispersion of water insoluble polymers which, on drying form an elastic film. There are four general classes of latex currently available, acrylic, styrene-butadiene copolymer, poly-vinyl-acetate/poly- vinyl-alcohol and natural latex isoprene. Unfortunately there is little work published in this area with the exception of Ichikawa *et al.*[1994], who have published works on both micro-encapsulation and granulation of powders with acrylic polymers in a Würster coater.

Ichikawa *et al.*[1994] found that for micro-encapsulation to occur without agglomeration the coating polymer must be deposited as a dry powder/film on the surface of the particle. This was achieved by the selection of a polymer with a softening point no more than 2^{0}C lower than the inlet air temperature. This ensures that coalescence of particles can not occur as there is not liquid available for bonding and the particles simple rebound following any collisions. While this eliminates agglomeration Ichikawa *et al.*[1994] found that the dry powder/film was highly permeable and offered little protection to the encapsulated powder. However, Ichikawa *et al.* over came this problem by producing nano-encapsulated copolymers prepared via coacervation. This formed nano-encapsulated copoly (12- ethyl acrylate, 6-methyl methacrylate, 4-hyroxyethly methacrylate) abbreviated to copoly-12-6-4, with a softening point of 26^{0}C, with a shell of copoly-6-12-8, with a softening point of 78^{0}C, which raised the softening point of the composite to 78^{0}C. The application of this composite coating to fine lactose, 53 to 63μm, produced poor encapsulation, as discrete particles of the coating agent where observed on the surface of the lactose.

The encapsulation was dramatically improved by curing the products at 80°C for 12hr. This allowed the encapsulated coploy 12-6-4 to be released as the shell of copoly-6-12-8 softened, thus sealing the surface of the lactose.

Ichikawa *et al.*[1994] also showed that particles of starch in the order of 10μm in diameter could be coated using the nano-encapsulated polymer system. However the gas velocity in the Würster coater had to be reduced from $0.8m^3$/min to $0.04m^3$/min to prevent excessive loss of particles via the filtration system and maintain particle recirculation. Conversely Ichikawa and Fukumori [1999] showed by lowering the softening point of a commercial product, Eudragit RS30D acrylic polymer, by the addition of a plastersizer, 5% triacetin, the softening point was lowered from 85°C to 65°C. This allowed the micro-granulation of pulverized phenacetin powder (D_{50} 8μm) using the Würster process to yield granules with mean particle diameters D_{50} of between 21 and 33μm, dependent on the binder flow rate. This further illustrates the effect of coating softening point and therefore viscosity on coalescence of particles.

The evidence of Ichikawa *et al.*[1994] and Ichikawa and Fukumori [1999] confirm the expected result of the viscous dissipation model, which predicts that agglomeration is highly likely for highly viscous polymer coatings unless the surface of the particles are free from liquid.

1.4 Prior Work

Preliminary studies in micro-granulation and micro-encapsulation have been carried out at Massey University. Brayshaw and Jones [1999] investigated granule quality as defined by granule size, size distribution, porosity and strength, produced in the spouted bed environment. Their investigation concerned the effects of binder type, binder viscosity, binder content, air-jet velocity, air temperature, system geometry, spray size distribution and spray-on rate. Spouted bed granulation proved difficult and the investigation was limited to design issues such as cone shape, air-jet velocity, fluidization, spray size distribution and spray rate. In their review of the design parameters, consideration was given to spouting stability, pressure drop, air jet velocity and atomizing the spray. The results of this investigation were general and qualitative in nature. They indicated the design problems encountered and the solution to some of these.

Following this work, Rynhart and Jones [2000] reviewed the theoretical conditions that determine the nature of particle interaction in the encapsulation and granulation processes. In addition, they investigated atomization and constructed a twin-fluid atomization system. A number of experiments were then carried out to determine whether granulation was viable using the modified apparatus. To overcome the drying limitation of the apparatus the operation of the process was carried out in stages, preheating followed by granulation and drying. Results were inconclusive but, as with Brayshaw and Jones, the work indicated problems encountered such as product loss during operation due to the poor efficiency of the filter system and a build up of powder on the base cone due to wetting by the atomized binder fluid.

1.5 Concluding Remarks

The review of current technology and coating models have revealed the Würster coating process to be widely used for the micro-encapsulation of powders as low as 10 microns in diameter [Ichikawa *et al.*1994]. However this process is limited to the use of coating agents that produce dry particle surfaces which prevents agglomeration occurring . The process of particle agglomeration or coalescence is described by two models, one based on the dissipation of the particle collision energy by the displacement of the surface layer of liquid during the collision [Ennis *et al.*1991], and the capillary suction model which describes the forces due to the formation of a liquid bridge between the two particles [Simons *et al.*1994]. Of these two models the viscous dissipation model dominates in coating processes when high viscosity coating agents are used. This is supported by the findings of Ichikawa *et al.*[1994] who define the transition from coating to agglomeration as the softening point of the polymer coating, this transition point is explained by the viscous dissipation model, which states that as the viscosity is higher the maximum collision velocity is high and therefore agglomeration is likely.

The Wüster coater system used by Ichikawa *et al.*[1994], was able to coat particle of 53μm in diameter. However, as the particle size reduced the air flow needed to be reduced to allow the particles to dis-entrain from the exhaust gas and return to the fluid/spouted region of the coater. As an additional limitation, the inlet air temperature must be less than 2°C above the softening point of the polymer, which also significantly reduces the drying capacity of the system and increases processing time.

2 Design

Würster or spouted bed coaters are capable of coating particles in the order of 10μm in diameter [Ichikawa *et al.* 1994]. However the particle circulation in these systems relies on the particles dis-entraining from the fountain zone and settling back to the spouted bed zone. This limits the gas velocity in the spout and fountain zone and thus the drying capacity of the system and coating rate. An alternative design is possible that re-circulates both gas and entrained particles. This is achieved by utilising the gas induction effect produced by a high velocity gas jet expanding into a large draft tube. In addition to this feature a side mounted bag filter is used to allow fine particles to return to the spouted bed in the down draft zone created by the inductor.

The high velocity gas jet also assists in reducing the coalescence of wetted particles which may occur in the spouted zone if the particle collision velocities do not exceed the maximum collision velocity of coalescence, as predicted by the viscous dissipation model, eqn 1.6. This model predicts that for a medium viscosity coating agent such as 30% PEG 6000 the collision velocity of 100μm limestone particles must exceed 1.56 m/s, while for paraffin oil the collision velocity must exceed 50.5 m/s. Alternatively the coating rate must be low so that the binder to solid ratio, b^*, is below the critical level, b^*_c, eqn 1.23, or the surface of the coating is dry.

The liquid coating agent must be evenly distributed throughout the mass of particles being coated and evenly over the surface of individual particles, for the assumptions used in the viscous dissipation model to apply. This may be achieved by atomizing the coating agent using a twin fluid atomizer to produce a large number of coating droplets relative to the solid particles. Thus increasing the required number of

coating collisions to reach b^*_c for any individual particle.

To meet these requirements the design of the apparatus is broken down into four sections:

2.1 Gas and solids entrainment, utilising a high speed gas jet in a spouted bed.

2.2 Atomizer design, to produce small droplets which dry quickly and produce a uniform coating.

2.3 Drying chamber in the form of a draft tube, to allow drying of particles during pneumatic transportation prior to returning to the spouted bed.

2.4 Disentrainment chamber and filtration of exhaust gas, to allow the return of fine powders to the spouted bed and prevent pollution.

The final design of the apparatus is shown in fig 2.1. The design criteria that contributed to this configuration are discussed in each of the ensuing sections.

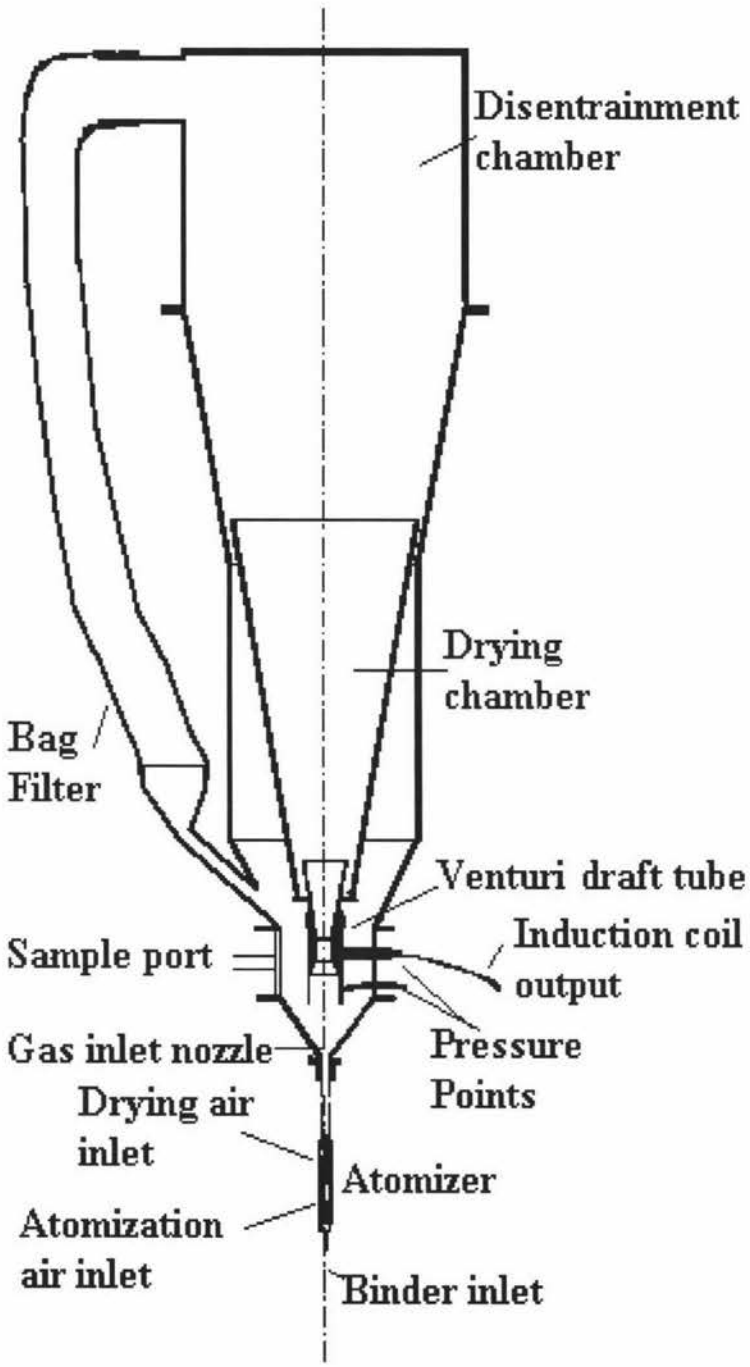

Figure 2.1 Apparatus design for spouted bed system.

2.1 Gas and Solids Entrainment

The air inlet nozzle and venturi draft tube are designed to perform three functions:

1. The entrainment of gas and solids to promote re-circulation in the apparatus
2. To increase gas velocity and turbulence
3. To allow measurement of the gas flow through the draft tube.

Gas entrainment

In traditional spouted bed systems relatively low inlet velocity gas jets are used to entrain solids in the spouted bed zone. The use of a high velocity gas jet and large diameter draft tube allows additional gas to be entrained into the draft tube by the jet. This effect is due to the entrainment of gas from the surrounding spouted bed and draft tube into the high velocity gas jet as it expands. This induces gas circulation in the system and provides additional gas flow for particle transport. The proposed system includes a venturi to improve particle and droplet mixing as they accelerate and decelerate through the throat of the venturi. An additional advantage of the venturi is that the gas flow through the draft tube can be measured easily.

The entrainment of gas and solids has been shown [Albertson *et al.* 1950; Yang and Keairns, 1982] to be a function of the inlet nozzle diameter $D_{j(0)}$, the initial mass flow of gas through the nozzle $Q_{g(0)}$, the gas dispersion angle θ, and the distance between the nozzle and draft tube z. Albertson *et al.* [from Tilton,1997] studied entrainment of gas from an unrestricted nozzle. For an angle of dispersion of 20^0, the maximum entrainment is expressed by equation 2.1, where $Q_{g(z)}$ is the total air flow at distance z.

$$\frac{Q_{g(z)}}{Q_{g(0)}}=0.32\frac{z}{D_{j(0)}},\quad for\ 7<\frac{z}{D_{j(0)}}<100 \tag{2.1}$$

The nozzle shown in Fig 2.1 is not unrestricted as it passes through a bed of solid particles prior to entering the draft tube where it expands into the draft tube entraining recycled air from the drying chamber. Particles are also entrained from under the edge of the draft tube. Within the core of the air jet nozzle there is a twin fluid atomizer that sprays liquid droplets into the air stream. As the air jet expands, the droplets and particles mix. To improve the turbulence and enhance mixing a venturi nozzle is placed just upstream of the draft tube. This forces the expanded air jet to compress slightly and gain velocity as it accelerates through the venturi.

The actual gas flow though the venturi can be measured easily by connecting a differential manometer to the draft tube inlet and venturi throat. The flow and pressure differential is related to the difference in cross-sectional area between these points and which changes the gas velocity. The design of the venturi to produce a pressure differential of 2 mm of water gauge, or 20 Pa, at a air flow of 0.0026 kg /s is achieved by the application of a simplified form of Bernoulli's equation for the conservation of energy, which ignores friction, change in gas density and gravitation potential energy, as given in equation 2.3.

$$\frac{P_1}{\rho_g}+\frac{U_1^2}{2}=\frac{P_2}{\rho_g}+\frac{U_2^2}{2} \tag{2.3}$$

Since the mass is conserved, the velocity of the gas, U, at point 1 and 2 are related by the ratio of cross sectional areas.

$$U_2 = U_1 \frac{D_1^2}{D_2^2} \tag{2.4}$$

In the design, a diameter ratio $D_1/D_2 = 2$ was used. Figure 2.2 shows the design of the venturi draft tube. An induction pickup coil was built into the throat of the venturi, allowing a magnetic particle to be detected for the measurement of particle circulation times and solids mass flow through the draft tube.

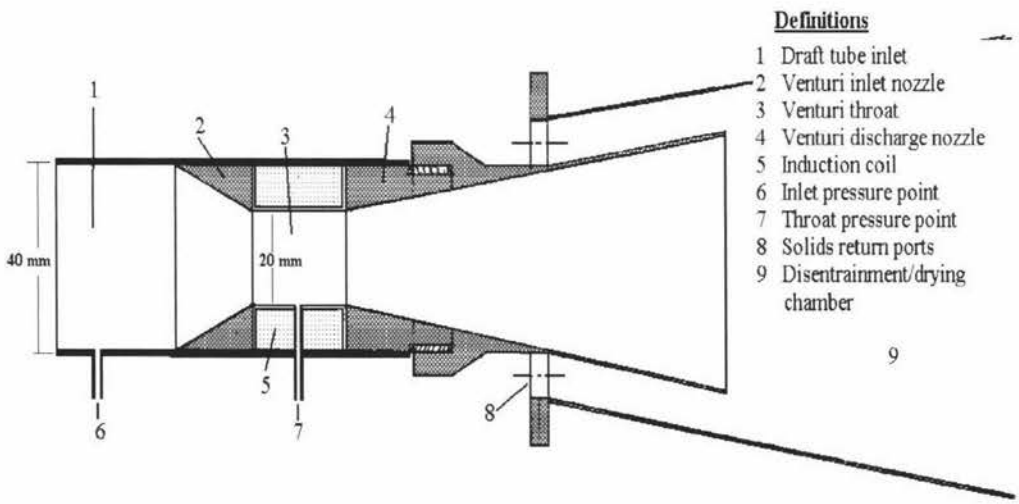

Figure 2.2 Venturi draft tube design.

The relationship between the velocity of the gas through the throat of the venturi, U_2, and the differential gas pressure, $\Delta P = P_1 - P_2$, and incorporating the design diameter ratio, $D_1/D_2 = 2$, eqns. 2.3 and 2.4 give the venturi throat velocity.

$$U_2 = \sqrt{\frac{2\Delta P}{\rho_g(1-\frac{D_2^4}{D_1^4})}} = \sqrt{\frac{32\Delta P}{15\rho_g}} \qquad \textbf{(2.6)}$$

The density of the gs under the operating tempra\ture can be obtained by applying a perfect gas correction to the STP(25°C, 1 atmos) density for air of 1.28 kg/m^3 . Equation 2.6 becomes.

$$U_2 = \sqrt{\frac{2\Delta P(T_g+273)}{357.6}} \qquad \textbf{(2.7)}$$

The denominator 357.6 in eqn 2.7 is the density of air at 298 K multiplied by the standard temperature 298 K and the venturi geometry factor (1- $(D_2/D_1)^4$).

This treatment of the venturi design excludes frictional losses due to wall effects, particle drag and the change in gravitational potential energy of the entrained solids. Due to this uncertainty, the venturi differential pressure response to flow was checked over a range of throat velocities from 2.0 to 22 m/s. This was carried out by attaching the inlet of the venturi to an air supply metered through a standard rotometer. The results of these trials, shown in Fig 2.3 are in good agreement with the calculated values, indicating that the frictional losses are small.

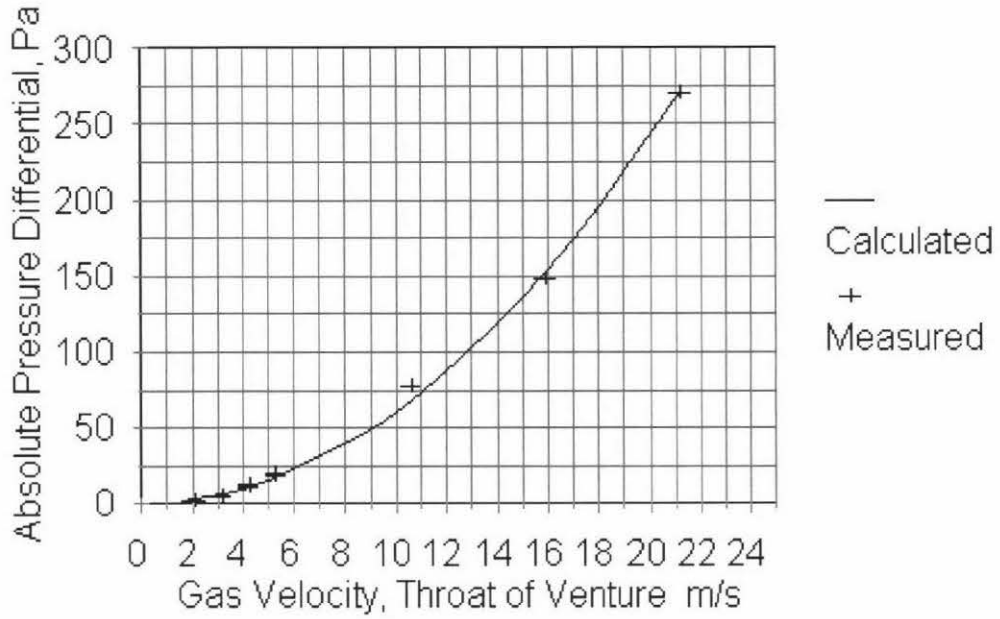

Figure 2.3 Correlation between calculated and experimental pressure differentials as a function of gas velocity through the venturi.

Entrained Air

The driving air is supplied from a lance placed below the inlet to the venturi. This driving air expands from the lance and entrains air as it advances towards the throat. The design of the venturi and draft tube allow the measurement of the entrained gas flow produced by the expanding gas jet which enters the draft tube from the fluidized bed. The maximum flow of gas can be predicted for the unrestricted expanding gas jet using eqn.2.1. This defines the total gas flow in the jet as a function of the inlet nozzle diameter, the distance from the nozzle and the initial gas flow. To confirm this effect the gas flow through the draft tube was measured as a function of inlet nozzle diameter and nozzle to draft tube separation distances, z, for nozzle diameters of 3, 5 and 7.7 mm positioned below the venturi throat, for inlet gas flows from 0.0006 to 0.0016 m^3/s. These results were then analysed using linear regression to determine the slope of the inlet gas flow versus the draft tube flow and are listed in Table 2.1.

Table 2.1 Gas entrainment results.				
Inlet Nozzle Diameter	Slope $Q_{g(z)}/Q_{g(0)}$ measured	z mm	Slope $Q_{g(z)}/Q_{g(0)}$ calculated	% Difference
3 mm	5.73	55	5.87	2.4
5 mm	2.86	51	3.26	12.2
7.7 mm	2.15	49	2.03	5.9

These results are in agreement with the coefficient of entrainment slopes predicted by equation 2.1 which defines the slope of the entrainment line as $0.32\ z/D_j$.

Solids entrainment

The entrainment of solids in the region between the nozzle and the draft tube is expected also to be a function of the separation distance between the draft tube and the air inlet nozzle, and the powder flow properties [Mathur & Epstein, 1974]. The entrainment of solids has been modelled by Yang and Keairns [1982] for high velocity gas jets entering a fluid bed of 2.8 mm diameter polyethylene beads. Figure 2.5 illustrates the model where a gas jet enters the base of the fluid bed and

expands at a half cone angle, θ, of between 7.5° and 10°.

As the jet expands through the fluid bed, along the z axis, solids enter the gas jet, increasing the rate of entrained solids, Q_s. The change in solids entrainment rate, dQ_s, is a function of the solid particle velocity in the z direction axis at point z, the radial particle velocity towards the jet v_r, the mass concentration of particles in the fluid bed, $\rho_s(1-\varepsilon_z)$, where ε_z is the voidage of the fluid bed at z, and the surface area at the interface area between the jet and the bed $2\pi r\ dz$.

These assumptions result in equation 2.7, which represents the instantaneous mass flux of solids entering the gas jet at point z. As r is a function of θ and the initial jet

$$dQ_s = v_r \rho_s (1 - \varepsilon_z) 2\pi r \, dz \tag{2.7}$$

diameter, D_j, equation 2.7 can be expressed in terms of these two additional factors.

$$dQ_s = 2\pi \rho_s (1 - \varepsilon) v_r \left(z \tan\theta + \frac{D_j}{2} \right) dz \tag{2.8}$$

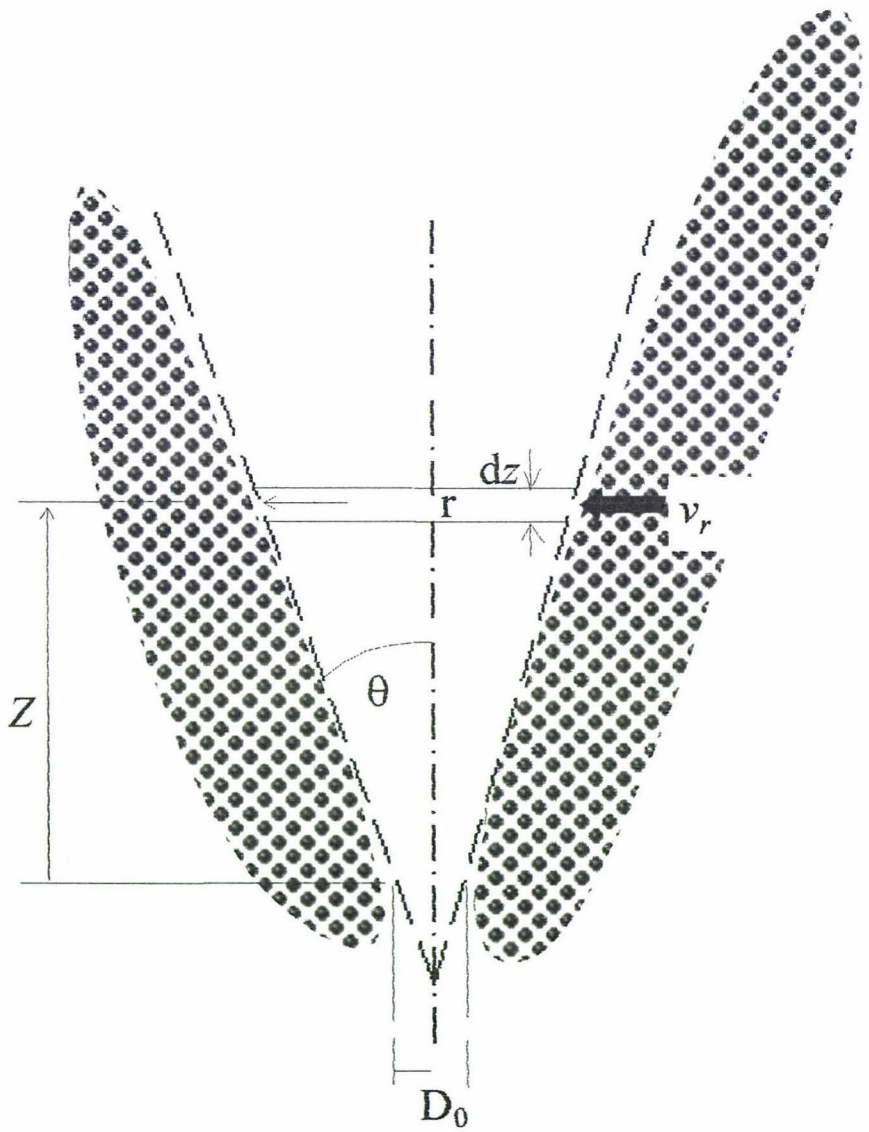

Figure 2.5 Solids entrainment into a spouted bed.

The integration of equation 2.8 then allows the calculation of the entrained solids mass flow, Q_s, to be calculated assuming v_r and ε are independent of z, which results in the model of Yang and Keairns [1982].

$$Q_s = 2\pi\rho_s(1 - \varepsilon)v_r\left(\frac{\tan\theta}{2}z^2 + \frac{D_j}{2}z\right) \tag{2.9}$$

This model does not take into account the particle collisions which may occur between particles in the jet and at the boundary, which may result in the rebounding of particles back into the bed. This occurs as the concentration of particles in the jet becomes high and limits the capacity of the jet to entrain solids.

As v_r is unknown, an assumption is made that the horizontal velocity component of particles entering the spout is the same as the horizontal velocity of a particle exiting a

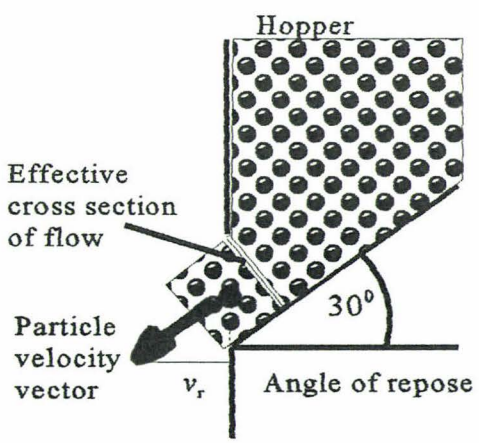

Figure 2.6 Horizontal velocity component of a particle leaving a vertical gate.

hopper through a vertical gate Fig.2.6. In this flow test apparatus a known weight of test product is placed in the hopper and the vertical gate opened. The time for the hopper to empty is recorded, thus allowing the mass flow and horizontal velocity component to be calculated. The horizontal velocity component of the particles was calculated assuming the particles exit the gate at an angle equal to 30 degrees, the angle of repose of the solids. The results of horizontal particle velocities are given in Table 2.2, for urea, short grain rice, fine salt and fine limestone. Theses results will be useful for later experimental work.

Table 2.2 Flow Test results for urea, salt ,rice and limestone.

Product and Size	Mass Flow Q_s g/s	Gate Area cm^2	Bulk Density $\rho_s(1-\varepsilon)$ g/cm^3	Horizontal Velocity v_r cm/s
Urea, 3.5 mm	55.5	8	0.704	7.2
Salt, 0.25 mm	113.7	8	1.129	9.3
Short Grain Rice, 2 x 5 mm	59.8	8	0.88	6.3
Limestone 30/200 mesh	80.28	8	1.2	6.1

This experimental approach is only an approximation. In a fluid bed, the solids density is lower than in a static bed. Therefore, the flowrate of material from a vertical gate represents the upper limit of horizontal velocity.

The horizontal velocity for rice can then be used to validate Yang and Keairns [1982] model using the solids mass flow data from Buchanan and Wilson [Mathur & Epstein, 1974] for wheat in a spouted bed with a draft tube insert. In these experiments a minimum inlet gas velocity of between 50 to 101 m/s was maintained as the draft tube separation distance from the nozzle was increased from 3.3 to 18.8 cm. As this is a

typical spouted bed, the inlet gas jet angle of dispersion is assumed to be zero, which describes a cylindrical spout interface commonly found in spouted beds. The diameter of the jet was given as, D_j = 1.27 cm while the bulk density and horizontal flow velocity for wheat and rice are assumed to be equal to those of rice given in table 2.2.

This allows the calculation of the mass flow of wheat as a function of the nozzle to draft tube separation. Figure 2.7, shows the comparison between the experimental data to the model.

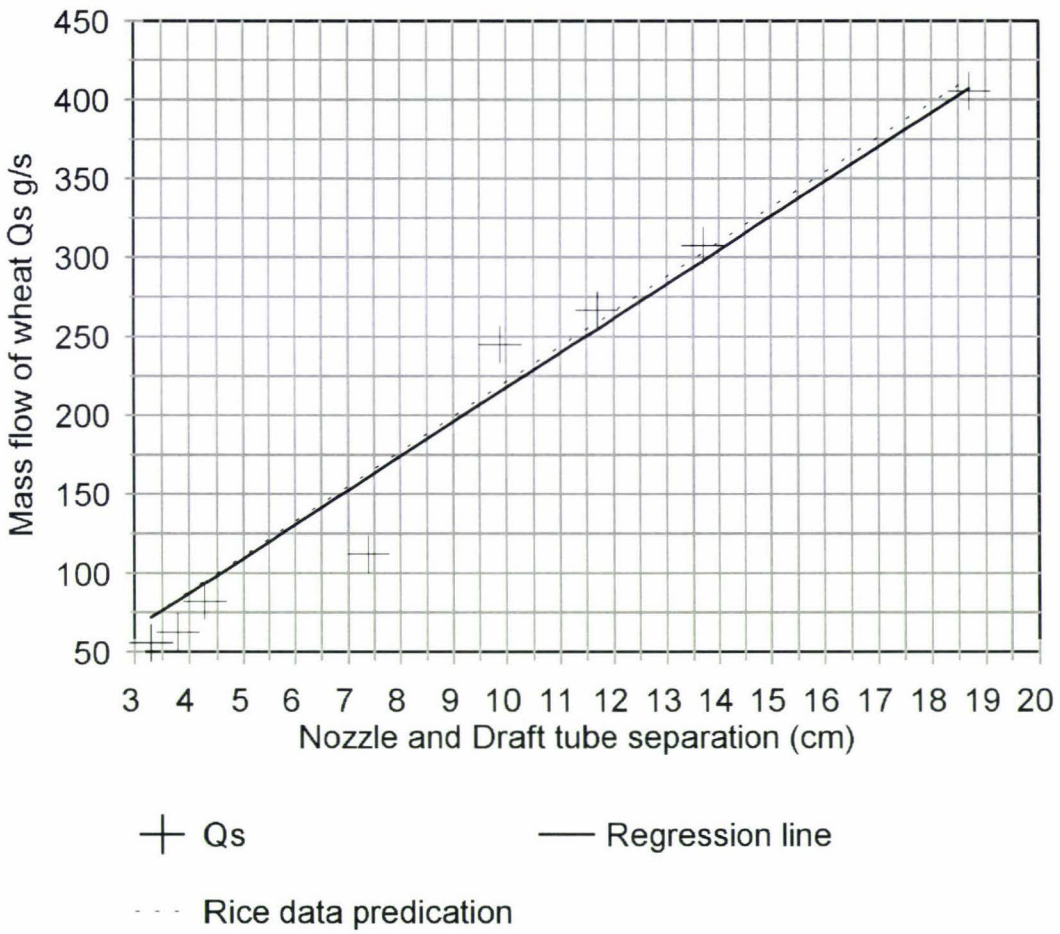

Figure 2.7 Analysis of wheat entrainment data [Buchanan and Wilson, 1965] using a modified jet entrainment model [Yang and Keairns, 1982].

The combination of gas and solids entrainment calculations allows the estimation of the maximum solids and gas mass flows through the draft tube, assuming no gas is entrained by the jet as it expands through the spouted bed. Based on this, the solid and gas entrainment were calculated for limestone 30/200 mesh (where no more than 30% of the particles are greater than 200 mesh in diameter) and an inlet air flow of 2 cm^3/s. Table 2.3 gives these calculations for the 5 and 10 mm inlet nozzles with a nozzle to draft tube separation of 55 mm and jet expansion angles of 0 and 10 degrees. The free jet entrainment figures can from equation 2.1. Air entrainment in a spouted bed or fluidized bed will be significantly less than predicted by eqn 2.1 because the presence of the bed restricts air movement. This calculation therefore represents an upper bound flowrate. The lower bound is calculable from air associated with the solids by multiplying the solids entrained by $\epsilon/(\rho(1-\epsilon)$. In reality, air flow will be somewhere between these limits because the fluid bed is not expected to occupy the entire separation distance from the nozzle to the venturi inlet.

Table. 2.3 Expected gas and solids entrainment results

Inlet nozzle, D_j, mm	Solids entrainment, g/s		Gas flow including free jet entrainment, eqn. 2.1 , cm^3/s	Gas flow entrained with solids, cm^3/s	
	0°	10°	10°	0°	10°
5	63	185	7800	2062	2021
10	126	249	3900	2083	2042

2.2 Atomizer Design

Previously in the discussion of particle coalescence, the critical binder to solids volume ratio, b^*_c, was defined by eqn.1.23. This estimates the maximum volume of binder which may be applied to the surface of a particle before the liquid layer exceeds the surface asperity height and coalescence becomes likely.

$$b_c^* = (1+\frac{h_a}{a})^3 - 1 \qquad \textbf{(1.23)}$$

This result is applied to determine the maximum binder droplet size necessary to avoid agglomeration during a coating process, given a particle radius a and the surface asperity h_a. For a smooth particle of 100 μm in diameter with a surface asperity of 0.5 μm , b^*_c is 0.015. Thus the droplet of binder must be no greater than 3/100 the volume of the particle volume, which is approximately 30 μm in this case. The probability of droplet to particle collision depends on the number ratio of droplets to particles, the turbulence, and the space distribution of droplets and particles. It is important to avoid mal-distribution of coating agent.

To achieve this droplet size range a concentric twin-fluid atomizer was developed, Fig 2.8, which consists of two nozzles arranged concentrically. This device contains a central liquid nozzle of 0.5 mm OD through which the binder solution is metered. Concentric to this is an atomizing air stream which supplies sufficient velocity to effectively atomize the binder. Concentric to both is a bulk air nozzle. The purpose of which is to provide drying air and momentum to circulate particles around the apparatus as shown in fig 2.1. This design allows the drying air, atomizing air and droplets to mix

just prior to entering the spouted bed. To allow loading of powder into the spouted bed apparatus the shaft containing the drying air and the atomizer nozzles is 150 mm long which allows it to be positioned inside the draft tube while solids are loaded into the apparatus.

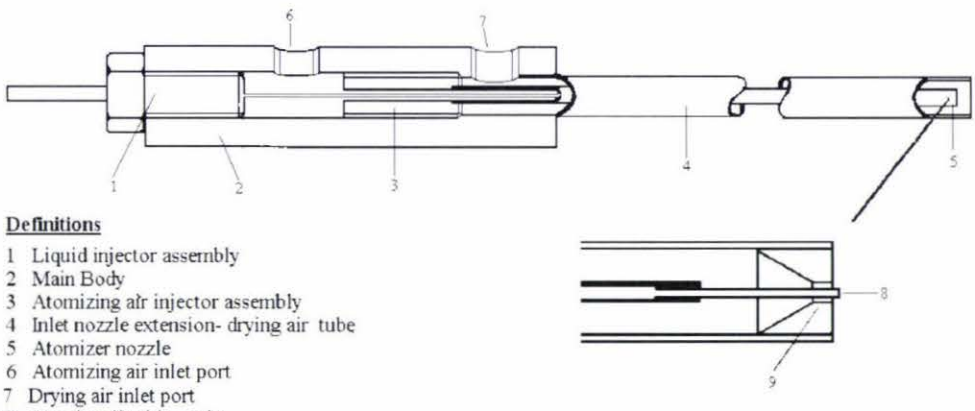

Figure 2.8 Atomizer and drying air nozzle assembly.

Empirically it has been observed that the mean mass droplet diameter, D_{50}, is a function of the relative gas velocity at the nozzle head V_{rel}, the mass ratio of air to liquid, Q_a/Q_l, and the viscosity and surface tension [Masters, 1976]. The minimum droplet size achievable with a two fluid nozzle atomizer is 5 μm which is achieved when V_{rel} approaches the speed of sound and Q_a/Q_l is between 6 and 15 for liquid viscosities of 5 cP to 250 cP respectively.

To determine the required mass flow of air, the mass flow of liquid must be calculated based on the drying capacity of the inlet air. An air rate of 0.002 m^3/s (0.0026 kg/s) at 80°C and 10% relative humidity has a drying capacity of 4.73×10^{-5} kg/s at maximum relative humidity of 70%. This was calculated based on the difference in absolute humidity, kg of water vapour / kg of dry air, between the inlet air conditions and the final air conditions for adiabatic drying using a psychrometric chart [Perry & Green,

1998, p.12-28]. The maximum humidity of 70% was selected to allow full drying of the potential coating binder solution. Thus the total permissible flow of 30% solids coating binder solution is 6.8×10^{-5} kg/s.

To achieve maximum atomization for a range of binder viscosities between 5 cP and 250 cP the mass flow ratio Q_a/Q_l must be between 6 and 15 , with a sonic (345 m/s) gas velocity through the gas jet [Masters, 1976]. Thus, the mass flow of air Q_a, must be between 4.08×10^{-4} kg/s and 1.02×10^{-3} kg/s to maximise the atomization of the maximum liquid flow Q_l, of 6.8×10^{-5} kg/s.

The diameter of the air nozzle was calculated to give a sonic or chocked flow based on the air flow of 6.33×10^{-4} kg/s at 3 bar gauge. As this nozzle is constructed around the 0.5 mm OD liquid nozzle, the area of the air nozzle A_a, was calculated using eqn 2.10, which determines the air nozzle area required for a mass flow of air, Q_a, of density of air, ρ_a and the the air velocity through the nozzle, v_a. For this design the air supply pressure is at the middle of operational range 3 bar and the gas density ρ_a is 3.48 kg/m^3, the speed sound v_a is 345 m/s. This calculated area is only an approximation because air is compressible and the density will be lower than stated for an adiabatic expansion.

$$A_a = \frac{Q_a}{v_a \rho_a} = \frac{6.33 \times 10^{-4} kg/s}{345 m/s \times 3.48 kg/m^3} = 0.527 \times 10^{-6} m^2 \qquad \textbf{(2.10)}$$

The total area, A_t, of the air nozzle orifice was then calculated by the addition of the air and liquid nozzle areas, this is equal to $(0.5272 + 0.1963) \times 10^{-6} = 0.7263 \times 10^{-6}$ m^2 . With the total area of the atomizer nozzle known, the overall internal diameter of the air nozzle was be calculated as 0.96×10^{-6} m or approximately 1 mm. This arrangement of a

0.5 mm OD liquid nozzle within an 1 mm ID air nozzle approximates the critical dimensions for maximum atomization of liquids with viscosities in the range of 5 to 250 cP according to the guidelines of Masters [1976].

Droplet diameter D_{50} and D_{90}

The analysis of the droplet size produced by the atomizer is required to ensure that it is operating in the required droplet size range of 90 % less than 30 microns as explained earlier. This was carried out using an optical imaging technique, due to the unavailability of more advanced techniques such as laser diffraction or scattering.

In this technique, a sample of the atomized spray is collected on a microscope slide and

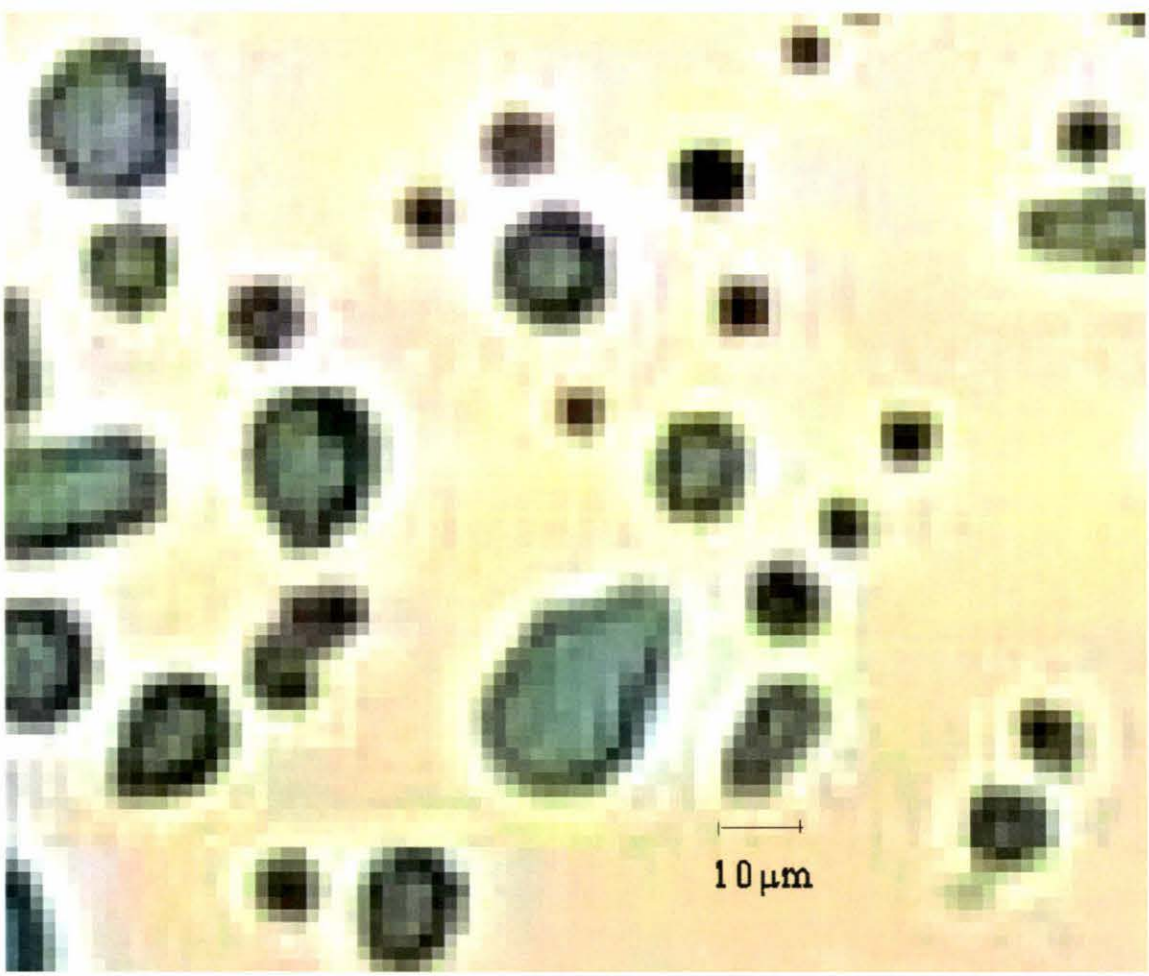

Figure 2.9. Bit map image of atomized 30% PEG + 5% dye solution using 6 bar air supply.

analysed using a microscope fitted with a video camera to obtain a digital image. The image was then analysed using the software package, SigmaScanPro, to measure the area of each individual droplet as pixel counts. The pixel units were calibrated against a standard grid and converted into microns. At the 10 x magnification one pixel was equal to 1.55 μm. Typically droplet images of 2 pixels or greater can be measured.

Figure 2.9 shows the resolution of the bit map image.As the droplets are spread over the surface of the glass slide an approximation of the droplet volume and diameter was calculated using equation 2.11 and 2.12, which converts the number of pixels into area (μm^2) by multiplying by 1.55. The droplet volume and diameter are calculated using the rough approximation that the deposited droplets are hemispherical with a contact angle of 90°.

$$Volume\ V_d = \frac{4\pi}{6}\left(\frac{1.55N_{pixel}}{\pi}\right)^{3/2} \qquad \textbf{(2.11)}$$

$$Droplet\ Diameter\ D_d = 4^{1/3}\sqrt{\frac{1.55N_{pixel}}{\pi}} \qquad \textbf{(2.12)}$$

The sampling of the atomized droplets required the construction of a "spray camera" as shown in Fig 2.10. This consisted of a sliding shutter, to limit the exposure time of the microscope slide to the spray, as over exposure resulted in drops coalescing on the slide.

In operation a microscope slide is taped to the back board in direct line of spray from the atomizer. The metal slide with absorbent pad is then positioned between the microscope slide and atomizer. The atomizer liquid and air flows are then set. The side is

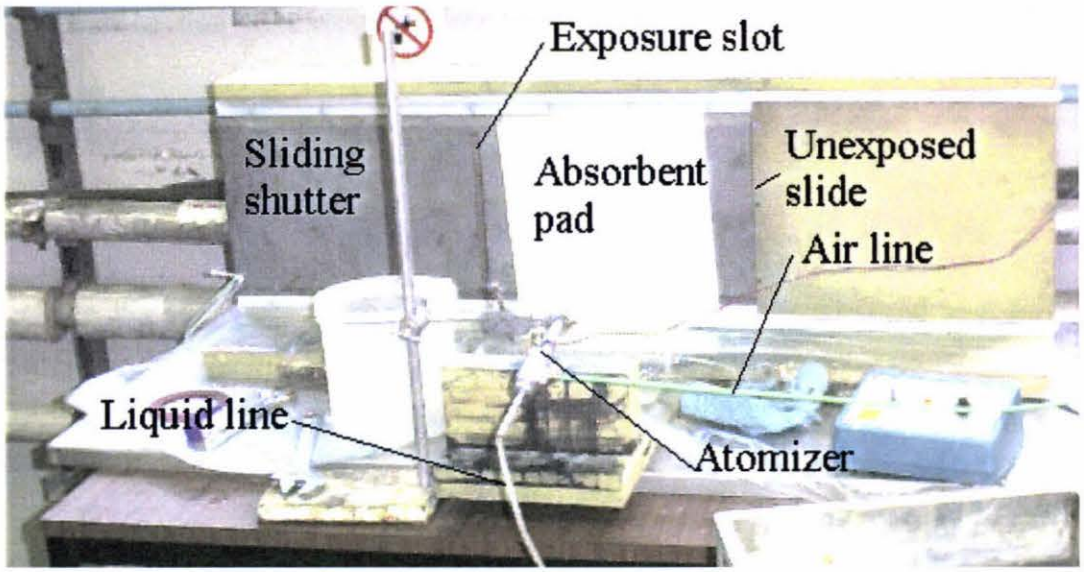

Figure 2.10 Spray camera

moved at constant velocity of approximately 1 m/s exposing the microscope slide as the 1 cm slit passes allowing approximately 0.01 second of spray exposure to occur. The atomizer is then shut down and the exposed slide removed from the back board and stored in a dust proof petri dish prior to viewing under a microscope.

The performance of the atomizer was determined in terms of D_{50} and D_{90} for mass flow of air of between 0.0011 kg/s to 3.2 x 10^{-4}, while the liquid flow was fixed at 6.67 x 10^{-5} kg/s, for 30% poly ethylene glycol 6000 with 5% Special Patent Blue dye in water. The results of these experiments are given in table 2.4 as droplet sizes as a function of Q_a/Q_l ratios from 4.8 to 16.9 and atomizer supply pressure.

Table 2.4 Atomizer performance.

Atomizer Air Supply Pressure Bar gauge	Q_a/Q_l	D_{50} microns	D_{90} microns
1	4.8	29	55
2	7.7	21	51
3	10.5	6	16
4	12.2	9	18
6	16.9	10	24

The results show that the optimum air to liquid mass ratio is 10.5 for the coating solution. Above this value, the D_{50} tends to 10 μm while the D_{90} increased. This broadening of the droplet size distribution may be due to droplet coalescence on the slide as seen in fig 2.8 or droplet coalescence induced by the increased turbulence in the atomizer exhaust.

Based on these results the atomizer was operated at a supply pressure of 3 bar over the range of the experiments.

2.3 Drying and Dis-entrainment Chamber

The solids which pass through the venturi draft tube must be dried prior to returning to the annular zone of the spouted bed or reaching the exhaust gas filter as wet product in these regions will cause the particles to stick together resulting in loss of fluidity in the annular zone or blinding of the filter. To achieve successful drying three components are needed; sufficient heat, air flow and particle(droplet)- air contact time in the drying chamber. The inlet air flow conditions are limited to a maximum flow rate of 0.0026 kg/sec of air at a maximum temperature of 80°C, with a humidity of 0.001 kg/kg dry air. Based on these conditions, the drying rate of the droplets must be calculated to allow the design of the drying chamber, which consists of the draft tube, particle dis-entrainment and return flow regions above the spouted bed.

Drying

As the droplets are small and the relative velocity between the droplet and air flow is negligible, the drying time was calculated in terms of heat and mass transfer balance, eqn 2.13 [Master, 1976], where ΔH_{vap} is the latent heat of vaporization, dM/dt is the rate of

mass change over time, h_c is the convection heat transfer coefficient, A is the surface area of the droplet and ΔT is the mean temperature differential between the droplet and drying air.

$$-\Delta H_{vap} d\frac{M}{dt} = h_c A \Delta T \qquad \textbf{(2.13)}$$

Equation 2.13 can be simplified because, under limiting quiescent conditions, the Nusselt number, N_u, (which is the total heat transfer over the conductive heat transfer) is approximately equal to 2.0, where k_d is the average thermal conductivity of the gaseous film surrounding the droplet.

$$N_u = \frac{h_c D_d}{k_d} = 2.0 \qquad \textbf{(2.14)}$$

By substituting $2k_d/D_d$ for h_c, πD_d^2 for A and investigating the drying of a single droplet M is replaced by $\pi D_d^3 \rho_l /6$ in eqn 2.13 and integrating this the drying time equation is obtained [Masters, 1976].

$$t = \frac{\Delta H_{vap} \rho_l}{8 k_d \Delta T_{LM}} (D_{d(0)}^2 - D_{d(f)}^2) \qquad \textbf{(2.15)}$$

The mean temperature difference between the droplet and drying air is taken as the Log mean difference eqn 2.16, where ΔT_0 is the initial differential temperature and ΔT_1 is the final differential temperature.

$$\Delta T_{LM} = \frac{\Delta T_0 - \Delta T_1}{\ln \frac{\Delta T_0}{\Delta T_1}} \qquad \textbf{(2.16)}$$

Applying equation 2.15, the drying times were then calculated for 500, 100, 50 and 10 μm droplets of water (Table 2.5) under the following drying conditions; ΔT_{LM} is 23, k_d the thermal conductivity of droplet(water) is 0.657 W/mK, ΔH_{vap} the latent heat of vaporisation(water) is 2.44 x 10^6 J/kg at 26°C and ρ_l the density of water is 1000 kg/m^3.

Table 2.5 Estimation of spray droplet drying times.

D_p initial(μm)	Drying time (s)
500	5.046
100	0.202
50	0.050
10	0.002

Based on this and the droplet size analysis, §2.2, the minimum particle-air contact time is 0.050 second however to be safe a drying time of 1 second was used in the design to ensure total drying of the product.

Particle dis-entrainment

The particles must be separated from the gas flow and allowed to return to the spouted bed zone of the apparatus for particle circulation to be continuous. This is achieved by dis-entraining the particles from the gas flow by lowering the vertical component of the gas velocity below the settling velocity of the particles.

Vertical pneumatic transport occurs when the force exerted on the particles by the viscous drag due to gas moving past the particle overcomes the gravitational force.

At this point the particle will be suspended by the gas flow. These forces can be expressed mathematically for a spherical particle where u refers to the relative velocity between the particle and the gas.

$$Viscous\ drag\ force = \frac{1}{8}\pi C_D \rho_g D_p^2 u^2 \quad \textbf{(2.17)}$$

$$Gravitational\ force = \frac{\pi}{6} D_p^3 \rho_s g \quad \textbf{(2.18)}$$

The coefficient of drag, C_D, is a function of the particle Reynold's number, $Re = (Du\rho_a/\mu_a)$. In semi-turbulent flow, when $0.2 < Re < 1000$, $C_D = 0.4 + 40Re^{-1}$. The substitution of these equations for C_D in the viscous force equation and equating the two force equation results in the expression of the terminal particle velocity in a quadratic form.

$$0 = 0.157\rho_a D_p^2 u^2 + 15.7\mu_a D_p u - 0.523\rho_s g D_p^3 \quad \textbf{(2.19)}$$

This force balance applies strictly to spheres and ignores buoyancy, but can be used if a compensation factor for non-sphericity is applied. The sphericity correction factors were obtained for ground limestone by direct measurement on the transportation gas velocities at particle sizes of 2(2.4x1.6)mm, 1.25(1.2x1.6)mm, 1 mm, 0.71 mm and 0.5 mm in diameter. The measurement was carried out by placing single particles in a vertical column fluid bed apparatus, the air flow was then increased until the particle became suspended by the air flow, at this point the flow rate was noted and the gas velocity in the column calculated. The results of these trials are given in Table 2.6.

Table 2.6 Disentrainment velocities and correction factor			
D_p mm	**v_t calculated m/s**	**v_t measured m/s**	**correction factor**
2	9.69	6.92-7.62	0.75
1.25	7.38	5.54	0.75
1	6.41	4.33-4.85	0.72
0.71	4.99	3.81-4.50	0.83
0.5	3.76	2.77-3.11	0.79

Based on these results a correction factor of 0.8 was used in the estimation of the dis-entrainment velocities for particles less than 0.71 mm and 0.75 for greater particles greater than 0.71 mm, as shown in Table 2.7.

Table 2.7 dis-entrainment velocities for limestone.

D mm	Dis-entrainment velocities U_t , m/s
2	7.27
1	4.81
0.9	4.49
0.8	4.13
0.7	3.99
0.6	3.53
0.5	3.02
0.4	2.42
0.3	1.72
0.2	0.51
0.1	0.27
0.05	0.07
0.025	0.04

With the minimum dis-entrainment velocities of 0.27 m/s for a 100 μm diameter limestone particle known, the draft tube and drying/dis-entrainment chamber were designed to allow at least 1 second of air-particle contact time, as it is reasonable to assume for small particles the drying time is equal to the gas retention time t_r.

The design of the draft tube and drying chamber is based on a conical section which allows the gas flow to slow with little turbulence. This is possible by expanding the gas in a conical tube which has a half angle of 10°, which is commonly accepted as

the maximum expansion angle at which a gas flow may be expanded without flow separation occurring at the wall. For design purposes the mean gas velocity can be assumed to reduce proportional to the cone diameter.

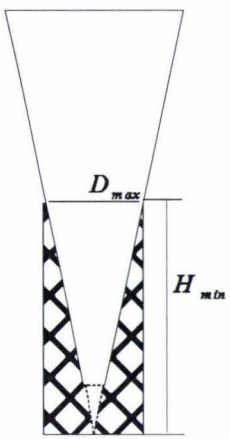

Figure 2.11 Geometry of conical draft tube design.

The dis-engaging particles recirculate to the fluid bed through the solids return ports (Fig. 2.2). This allows the gas to expand without excess turbulence. The conical draft tube Fig 2.11 has a minimum height, H_{min}, and maximum diameter, D_{max}, which allows the transportation and drying of the coated particle. The values of H_{min} and D_{max} are defined by equation 2.18 and 2.19. Equation 2.18 defines the diameter of the draft tube based on the volumetric flow of gas is Q_g/ρ_g and the cross-sectional area required for the gas velocity to fall below the settling velocity of the particles, U_t,. While the minimum height required is defined by the volume of a tube of diameter, D_{max}, equal to the volume of gas required to achieve the drying time is , t_r . These two equations satisfy both the drying and particle transportation requirements for the system.

$$D_{\max} = 2\sqrt{\frac{Q_g}{\pi \rho_g u_t}} \tag{2.18}$$

$$H_{\min} = \frac{12 Q_g t_r}{\rho_g \pi D_{\max}^2} \tag{2.19}$$

The application of these equations to the estimated gas flows of between 0.002 and 0.006 m^3/s and a particle size of 100 μm, shows that the maximum diameters for the outlet of the draft tubes are 97 and 168 mm, with total drying chamber volumes of 2 and 6 litres respectively and a minium draft tube height of 270 mm in both cases.

The dis-entrainment of fine particles less than 25 μm is required to reduce the solids loading on the filter unit. The settling velocity of these particles is 0.02 m/s, which translates into a chamber diameter of greater than 250 mm based on the exhaust gas flow of 0.002 m^3/s. However, small particles are increasingly affected by turbulent eddies within the air flow and therefore these calculation must be considered in context.

Figure 2.1 shows the design of the conical draft tube and dis-entrainment chamber. The initial stage of the draft tube is an extension of the venturi exhaust, which terminates inside the secondary stage, the conical section, which allows larger particles to disentrain from the main gas flow. Slots in the wall allow the particles to fall through to the spouted bed zone. With the above disentrainment considerations the outlet diameter of the secondary conical section was selected to be 200 mm, which corresponds to an average gas velocity of 0.190 m/s meaning that particles greater than 75 μm will disentrain in the conical section. Smaller particles will pass into the upper section called the fine particle dis-entrainment chamber. This upper section has a conical base expanding to 300 mm allowing 25 μm particles to disentrain (assuming laminar air

flows). The upper section also contains the main gas re-circulation slots that further reduce the airflow prior to the filter port in the top most part of the chamber. The air flow is expected to drop from 0.006 m^2/s at the draft tube exit to 0.002 m^2/s at the filter. The remaining solids are then removed by the bag filter and are returned to the spouted bed zone as shown in figure 2.1.

2.4 Filter

Filtration of the exhaust gas is achieved using a bag filter connected to the topmost chamber with the fine particles discharged to the spouted bed (Fig. 2.1).
This design reduces the accumulation of fine particles on the filter fabric and allows for periodical mechanical cleaning while the apparatus is operating.

The fabric bag was made from 100% polyester chiffon 125 g/m^2 formed into a 100 mm diameter tube and 1 metre long. Polyester was chosen due to its high operating temperature, 120^{0}C, and resistance to swelling at high humidity . The required area of the filter bag was determined based on [Perry & Green, 1997, p.17-42 to 17-46] the specific resistance of the fabric and the powder loading on the surface of the fabric at the superficial gas velocity, equation 2.20,

$$\Delta P = K_f U + K_p \omega U \qquad \textbf{(2.20)}$$

where ΔP is the pressure drop across of filter in Pa, K_f is the coefficient of resistance for the fabric, U is the superficial gas velocity, K_p is the coefficient of for the resistance for the powder and ω is the powder loading in kg/m^2. For a solids loading of $\omega = 0.196$ kg/m^2 Perry and Green give K_f as 41.1 kPas/m for a Dacron filter and K_p between 190 and 270 kPa s m/kg when the solids are less than 25μm in size. The powder loading of

the fabri, M_{sf} was estimated based of the quantity of particles less than 25μm which may be entrained in the gas flow and deposited on the filter. For design the powder load of 300 g with 10% of the particles less than 25 μm yields a maximum solids loading of 30 g on the area of the filter. As $\omega = M_{sf}/A_{filter}$ in equation 2.20, the area of the filter is adjusted until the pressure drop across the filter is within its design limits and the limits of the available air supply.

Thus the filter of 0.314 m^2 with an estimated powder loading of 0.02 kg/m^2 and a superficial gas velocity of 0.382 m/min should have a pressure drop of 258 Pa which is acceptable in this application.

2.5 Instrumentation

To determine the operational characteristics of the designed coating system, an instrumentation system capable of measuring; flows, temperatures and pressures, simultaneously at fourteen individual points is required. Figure 2.12 shows the instrumentation selected to monitor the operating conditions.

The data acquisition system was developed to consist of four main components:

1. Sensors or transducers
2. Conditioners
3. Analog to digital converters ADC
4. Computer

Each of these components were selected for compatibility and accuracy.

producing a change in output voltage. The output voltage can then be amplified using an operational amplifier to the required level for data acquisition.

The pressure sensors perform two functions:

1. determine system pressures
2. measure gas flows through the venturi by recording differential pressures.

Temperature sensors

The determination of temperature in the system was achieved using T-type thermocouples. This type of sensor produces a voltage output as a function of the thermal migration rate of electrons across the junction of two metals, copper and constantan. The voltage is measured relative to a standard cold junction which acts as a reference. The voltage output typically varies by 4.3 mV between zero and 100°C, and requires amplifying for data acquisition.

Humidity sensors

Humidity sensors were required to measure the water content both in the incoming air and in the internal system air. This allows the drying rate to be calculated, and indicates when the system is becoming saturated with water. The humidity is a Honeywell capacitive type with integrated signal conditioning. This produces a 0.8 to 3.9 V DC output over the range of zero to 100% RH and can be directly measured.

Gas flow sensors

Three types of gas flow sensors were used in this system to the measure the input air flows and the total internal gas flows. The input drying air flow was measured prior to the heater using an analog in-line turbine gas flow meter, modified to allow a voltage output to be taken from the analog display terminals. This voltage was then amplified to give a reading of 1 V DC at 100 l/min of gas flow.

The atomizing air flow was measured using a critical flow nozzle fitted with a supply pressure sensor. In this type of system the flow rate is a function of the gas density, nozzle diameter and frictional losses. Thus, the flow is proportional to the supply pressure for a given nozzle. This nozzle was calibrated against a standard gas flow rotameter to obtain a calibration between the supply pressure and flow.

The gas velocity, U_g, which passes through the venturi was measured using a differential pressure sensor between the inlet and throat of the venturi. As this pressure differentials was very low, about 20 Pa at 100 l/min, a sensitive pressure sensor manufactured by "Sensor Techniques" was used, with a zero to + 5 mbar operating range. This sensor produces a 0.5 to 4.5 V DC output over 5 mbar, which was reduced to 2.5 V DC over a resistor bridge giving a full scale response on the analog to digital converter (ADC).

Weight sensor

The binder flow Q_b was determined by measuring the change in weight of the supply reservoir mounted on a load cell. The load cell operates on a similar principle to the pressure sensor but instead of the change in resistance of a piezo-material, the change in resistance is measured with four strain gauge resistors positioned on a deformable beam. The strain gauge resistors are made from very fine resistance wire glued to the surface of the beam. As the beam bends under a load, the wires are stretched and the resistance changes, allowing a voltage change to be measured. The load cell has a maximum load rating of 5 kg and a sensitivity of 0.02 g after amplification of the signal.

Induction sensor

This sensor was developed for this project to detect the passage of a 0.4 mg magnetic particle as it passes through the venturi of the apparatus. This allows the circulation

time, t_{circ}, to be measured. The sensor consists of a 40 kΩ, 0.2 mm copper wire coil wound around a 20 mm internal diameter spool insert, which makes up the throat section of the venturi. This coil also acts as a low pass filter, which reduces the signal noise prior to amplification. After amplification, the signal was used to trigger a one volt optical linked relay, which carries the signal to the ADC. The duration of this pulse is in the order of 100 ms thus requiring a high speed ADC for data acquisition. This was a separate requirement to the other sensors, which do not need high speed resolution.

Conditioning of sensor outputs

The wide range of sensors used in this system have varying outputs from mV to 5 V. This meant that the output signals from the sensor must be conditioned to within the range of the selected ADC to allow the required level of resolution to be obtained. Two forms of conditioning were used in this system to produce full scale input signals of zero to 2.5 V for the ADC. Signals were amplified using AMPO-4 instrumental operational amplifiers and for voltage reduction a resistor bridge was used. The details of the required conditioning are given in Table 2.8 below.

Table 2.8 Instrumentation summary.			
Position	Model No.	Conditioner Gain	Output
Atomizing Air Pressure	HW 24PCFFMIG	X 83	2.5 V / 100 psi
Secondary Air Pressure	HW 24PCFFMIG	X 83	2.5 V / 100 psi
Binder Flow	Unknown model	X 500	2.5 V / kg
Venturi Flow	ST HCXPM005D6V	X 0.625	2.5 V / 5 mbar
System Pressure	HW 26PCBFA16	X 83	2.5 V / 50 in WG
System Humidity	HW HIH3602A	1	1V / 100% RH
Drying Air Flow pre-Heater	unknown	X 38	2.5 V / 100 l/min
Drying Air Pressure	HW 26PCDFA1G	X 38	2.5 V / 30 psi
Drying Air Humidity pre-Heater	HW HIH3602A	1	1 V / 100% RH
Magnetic Particle Detector	triggered output	1	1.5 V max

Note. Model No., HW = Honeywell, ST = Sensor Technics

Analog to digital converter ADC

The large number of sensors in this system required thirteen channels of data to be collected with each channel having varying requirements for resolution and sampling time. These conditions were meet by using a combination of four ADC's; two Pico-ADC-16(for high resolution measurement of gas and binder flows, pressures and humidity), a Pico-TC-O8 for direct measurement of unconditioned thermocouple inputs, and an Pico-ADC-10 for high speed measurement of the signal from the induction sensor. Table 2.9 gives the sensor positions, type, resolution requirements, sampling rate requirements and bit resolution of signals required.

Table 2.9 Sensor details.				
Position	Type	Resolution	Sampling rate	Bit resolution
Atomizing Air	Pressure/Flow	0.1 psi	1 s	12
Secondary Air	Pressure/Flow	0.1 psi	1 s	12
Binder Flow	Load Cell	0.02g	1 s	16
Venturi Flow	Pressure/Flow	1 l/min	1 s	10
System Pressure	Pressure	5 mm WG	1 s	10
System Temperature	Thermocouple	0.1 deg C	1 s	#
System Humidity	Capacitive	1%/ 1mV	1 s	12
Drying Air Flow pre-heater	Flow	1 l/min	1 s	10
Drying Air Pressure	Pressure	0.1 psi	1 s	10
Drying Air Temp pre-heater	Thermocouple	0.1 deg C	1 s	#
Drying Air Humidity pre-heater	Capacitive	1%	1 s	12
Drying Air Temp post-heater	Thermocouple	0.1 deg C	1 s	#
Magnetic Particle Detector	Induction	0.1 V	0.01 s	8
Product Temperature	Thermocouple	0.1 deg C	1 s	12

The Pico systems of ADC were selected on the basis of the compatibility of the associated software and display the key process sensors graphically during an experiment. One downfall of this system is that, due to the serial acquisition of data on the ADC-16 and TC-08, the sampling speed is limited to the sum of the acquisition times. Thus, the high speed data collection from the magnetic particle detector required a separate ADC and software to achieve the required sampling rate.

Computer system

The computer requirements to allow the rapid collection and storage of data are based around the number of ADC's and the software. This required a computer with 3 available serial comports for the ADC-16's and the TC-08, and a parallel port for the ADC-10.

The computer must also run Windows and DOS software simultaneously in order to log rapidly from the ADC-10 using a DOS version of the Pico software.

Based on these requirements, a computer system was constructed based around a Pentium 75 MHz processor with, four serial comports, a parallel printer port and a 3.5" floppy drive for data transfer and backing up functions.

Calibration

All the sensors in the system required calibration against known reference standards:

- The high pressure sensors were calibrated using a dead lift hydraulic tester while the low pressure sensors were calibrated against water columns.
- The humidity sensors were supplied with calibration charts, but these were checked against standard humidity solutions of saturated K Cl at 76% RH and dry silica gel

  0% RH to ensure the accuracy of results.
- The load cell output was calibrated against known weights to obtain a calibration curve and optimize signal conditioning.

The following tables 2.10-2.17 list the calibration of the various sensors.

Pressure sensor calibration and conditioning

Table 2.10 Drying Air Pressure

Drying Air Pressure model HW 26PCDFA1G			
Pressure psi	10	15	30
Conditioned Output Voltage	0.84	1.25	2.5
Mean response V/psi	0.08	0.083	0.083

Table 2.11 Atomizing Air Pressure

Atomizing Air Pressure model HW 24PCFFMIG					
Pressure psi	20	50	60	80	100
Conditioned Output Voltage	0.53	1.26	1.5	2.01	2.51
Mean response V / psi	0.02 6	0.02 4	0.02 5	0.02 5	0.02 5

Table 2.12 Secondary Air Pressure

Secondary Air Pressure model HW 24PCFFMIG					
Pressure psi	20	40	60	80	100
Conditioned Output Voltage	0.47	0.97	1.5	1.965	2.5
Mean response V / psi	0.02	0	0	0.02	0

Table 2.13 System Pressure

System Pressure model HW 26PCBFA16						
Pressure mm H_2O	0	38.1	88.9	508	991	1257
Conditioned Output Voltage	0	0	0.1	0.76	1.75	2.5
Mean response mV/mm H_2O		1	0.7	1.5	1.7	2

Table 2.14 Load cell

Load cell				
Weights in grams	0	3.74*	17.22	274.2
Conditioned Output Voltage	0.96	0.9658	0.9778	1.233
Conditioned Output Voltage	0.961	0.9654	0.9778	1.2338
Conditioned Output Voltage mean	0.961	0.9656	0.9778	1.2334
Mean response mV/ gram		1.004	1.004	0.995

* during this series of measurements at 3.72 grams the base voltage changed to 0.9617

Table 2.15 Venturi Flow Pressure Sensor

Venturi Flow/ Pressure Sensor	model ST HCXPM005D6V					
Pressure mm H_2O	0	2	12	28.5	45	56.3
Conditioned Output Voltage	0.83	0.69	0.9644	1.194	1.276	1.55
mean response mV/ mm H_2O			11.6	12.92	10.02	12.8

* The pressure can then be convected to the gas velocity in the venturi throat via the equations 2.6 and 2.7

Calibration of critical flow nozzles

The critical flow nozzles were calibrated against the turbine flow meter using the pressure reading from the Pico data acquisition system. The flow is measured at standard condition S at 1 atmosphere and 25 degrees C.

Table 2.16 Atomizer Gas Flow Nozzle

Atomizer Gas Flow Nozzle			
Operating Pressure psi	20.3	31	50.59
Gas Flow SL/min	12.8	18.6	28.7
Ratio Sl/min per psi		0.542	0.515

Table 2.17 Secondary Air Flow Nozzle

Secondary Air Flow Nozzle					
Operating Pressure psi	0	19.2	40	63.5	76.5
Gas Flow Sl/min	0	20	40	60	70
Ratio Sl/min per psi		1.04	0.96	0.85	0.77

Conversion factors for voltage outputs to engineering units

The results of the calibration studies allowed the conditioned sensor output voltages to be converted to engineering units such as flows in l/min, pressures in kPa and weight in grams. Table 2.18, lists the sensors and their conversation factors and estimated errors

as defined by the variation in sensor responses results from the mean result, expressed as the % relative standard deviation, %RSD, or coefficient of variation.

Table 2.18 Voltage to Engineering Units Conversion Table.

Sensor	Conversion	Conversion factors	Error in Coefficient %RSD
Atomizing Air Pressure	volts to l/min	V x 20.7	5%
Secondary Air Pressure	volts to l/min	V x 37.2	5%
Binder Flow	mV to grams	mV x 1.0	0.5%
Venturi Flow	mV to m/s	(2x(mV*11.3)x((T_g+273)/360.4)^0.5,3 %RSD	
System Pressure	V to kPa	V x 0.0135	36%
System Humidity	V to %RH	V x100	+ 1%
Drying Air Flow pre-heater	V to l/min.	V x 1	+ 2%
Drying Air Pressure	V to kPa	V x 0.117	0.5%
Drying Air Humidity per-heater	V to %RH	V x 100	+ 1%
Magnetic Particle Detector	V	Pulse < 0.5V= Pulse	NA

The observed errors in the calibrated data are significantly higher than the specifications for the sensors, but are all within acceptable levels. The errors are caused, not by the sensor specifications, but by the calibrations. The system pressure error is high at 36% RSD, but still acceptable because it indicates over-pressure in the system. The poor response given by this sensor is due to incorrect selection as the rate range is 0-5 psi, while it has been calibrated to give full response over 0.2 psi thus, resulting in poor sensitivity.

Calculation of gas properties

The gas viscosity μ_g and density ρ_g of the gas passing through the venturi are calculated based on the temperature only, as the change in gas composition due to water vapour is only 1.5% over the full range of experiments. The gas viscosity is related to the temperature using the collocation derived from Beerman's table [Perry & Green., *1997*].

$$Viscosity\ Nsm^{-2} = 10^{-6} \times e^{(T \times 0.00184 - 2.855)} \qquad \textbf{(2.21)}$$

Viscosity $Nsm^{-2} \times 10^{-6}$	18.33	19	20	21
Temperature deg. C	27	50	80	100

The gas density ρ_g is calculated from the perfect gas equation as a function of gas temperature(as used to determine eqn.2.7).

$$\rho_g = \frac{1.29 \times 298}{T_g(^0C) + 273} \qquad \textbf{(2.22)}$$

3 Experimental

The effectiveness of the design was tested experimentally in terms of the mass flow of solids through the draft tube and gas entrainment rate. To preliminary campaigns of experiments were carried out.

The mass flow of solids through the draft tube was determined as a function of inlet gas nozzle diameters of 5 and 10 mm, and solids loadings of 100 and 300g respectively. This measurement allowed the binder to solid volume ratio b^* to be calculated which was used to predict whether coating or coalescence dominates the granulation process.

The gas entrainment rate into the expanding gas jet was determined as a function of solids loading in the system and nozzle diameter for a fixed inlet gas flow and nozzle to draft tube separation, by the measurement of total gas flow through the draft tube. These results allowed an improved estimation of the gas circulation rate and the gas to particle contact time for drying.

Following these preliminary experiments granulation and coating experiments were carried out to determine :

1. The dependency of granule growth rate, G, on the three adjustable variables, binder flow, Q_b, inlet nozzle diameter, D_j, and the total mass of solids in the system, M_s.
2. The encapsulation efficiency of the system was assessed by coating fine salt, sodium chloride with a mean particle diameter of 250μm, with a composite mixture of acrylic polymer, Eudragit NE 40D and Bentonite clay in the form of a 13% suspension in water. The effectiveness of the coating was then determined by the measurement of the extraction rate of sodium.

3.1 Mass Flow Rate of Solids

The mass flow rate of solids through the draft tube was expected to follow the model of Yang and Keairns [1982], as given in equation 2.9.

$$Q_s = 2\pi\rho_s(1 - \epsilon)v_r\left(\frac{\tan\theta}{2}z^2 + \frac{D_j}{2}z\right) \quad .$$

The mass flow is dependent on the bulk density of particle in the bed $\rho_s(1-\varepsilon)$, the radial velocity of the particles v_r, the nozzle diameter D_j, and the separation distance between the draft tube and the nozzle z, which was fixed at 55 mm. Of these factors only the diameter of the inlet nozzle, D_j, was adjustable at two levels 5 and 10 mm, while the other factors were known or constant. The radial velocity was given in table 2.2, calculated for the gravity flow of limestone through a vertical gate which simulates the transportation of powder into the entrainment zone. The bulk density was also taken from table 2.2 and assumed a non-fluid flowing solid bed.

The measurement of the mass flow was made by the addition of a magnetic particle to the system while the powder circulated. The circulation time of this particle was determined by the measurement of the time interval between signals induced in the coil as it passes through the throat of the venturi. This indicated the mean circulation time of the powder allowing the mass flow rate to be determined based on the total mass of solids in the system.

The signal induced in the coil by the magnetic particle was amplified using a AMO-4 operational amplifier with an adjustable gain from 1 to 1000 and a maximum voltage output of 9V. The amplified output signal was then filtered using a adjustable voltage trigger circuit and converted to a digital signal using a high speed Pico ACD-10

analog digital converter which was optical coupled to the recording computer. As the detection system was very sensitive, and capable of detecting biological EMF levels, the gain and trigger voltages were optimized for the particle detection and to reduce stray electrical noise. The main source of electronic noses which swamped the magnetic particle single was created by the power supply transformer for the heater and instrumental signal conditioners. These were turned off to allow the detection of the circulating particle once stable operating conditions were reached. During the circulation time experiments, the inlet gas flow meter and the shaker were operated as they had independent power supplies. This allowed the inlet gas flow to be controlled during the experiments and the particle flow to be stabilised by the shaker action.

The magnetic particle was prepared by encapsulating a 10 to 50 mg fragment of Alnico or similar magnet in hot glue, to form a 1 to 1.5 mm diameter particle. The encapsulation and enlargement of the particle was required to prevent the particle adhering to the slightly ferromagnetic areas in the stainless steel body of the apparatus. These areas resulted from welding and stressing of the metal during the fabrication process.

To determine the effect of the nozzle diameter on the solid flow through the draft tube the particles circulation times were measured for 100 and 300 g loadings of granulated limestone, with an initial particle size less than 2 mm in diameter. The granulated limestone allowed the circulation to be established rapidly and the magnetic particle to be introduced via the sample probe. The granules then broke down during the particles circulation to give fine powder which was similar to the powder size used to produce the granules. The inlet air flow was maintained at 130 l/min during the experiments, with 100 l/min of room temperature drying air and 30 l/min of atomizer air

flow. The nozzle to draft tube separation was 55 mm.

The results of the four trials are shown by Figures 3.1 as cumulative circulation time frequencies and in table 3.1 as median circulation times and mass flow rates.

Table 3.1. Summary of particle circulation trial results		
Trial Conditions $M_s(g)/D_j(mm)$	Particle Circulation Time (s)	Mass Flow of Solids Q_s kg/s
100/5	1.2	0.083
300/5	2.9	0.1
100/10	1	0.1
300/10	3.1	0.096

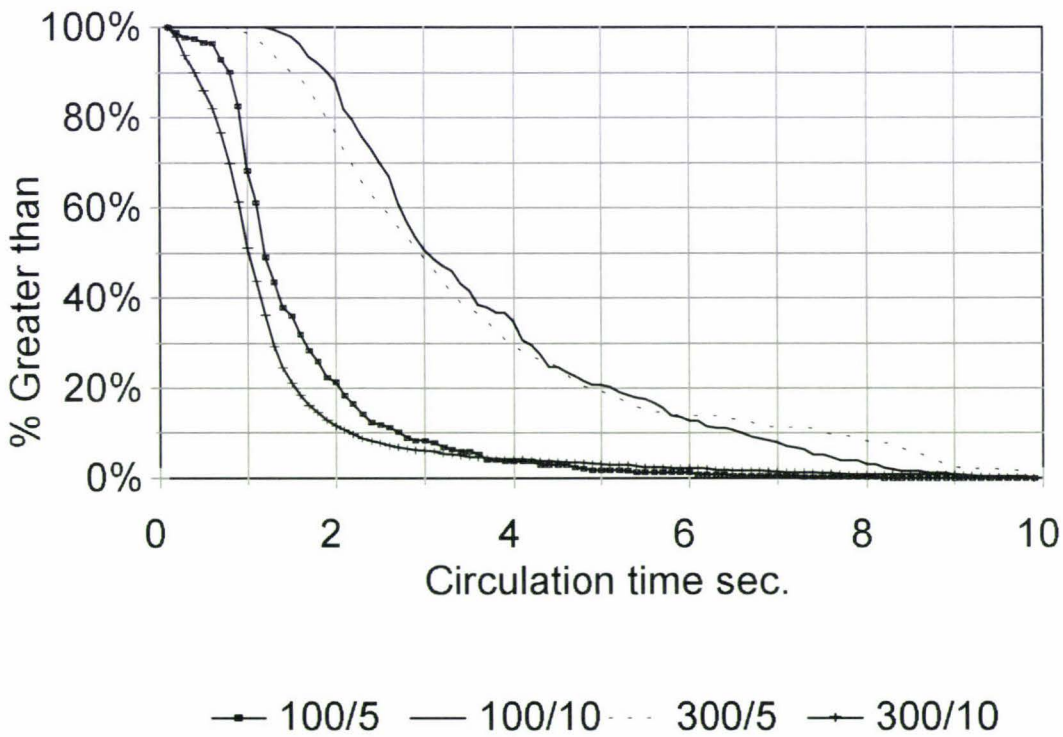

Figure 3.1 Cumulative frequency and time plot of particle circulation times.

The results showed that the particle circulation time was proportional to the total mass of solid, and relatively independent of the inlet nozzle diameter. The total flow of solids

was found to be closed to those predicted for a jet expansion angle of 0° (see table 2.3). This means that the gas jet did not expand in the bed region which was in agreement with the analysis of mass flows for wheat in a spouted bed [Buchanan and Wilson, 1965].

From the solids and gas flows the maximum value of the binder solids ratio, b*, was calculated to be ~0.002. This was obtained from the calculated solid volume recirculation for limestone of 39 cm^3/s and the drying capacity of the inlet air, which is able to dry 0.068 cm^3/s of binder solution containing 30% polyethylene glycol. The solid volume recirculation was calculated from the average mass flow of 0.094 kg/s from table 3.1 and the density of limestone, 2400 kg/m^3. The drying capacity of the inlet air with flowrate 0.002 m^3/s is calculated in Section 2.2.

The critical binder to solids ratio, b_c^*, where coalescence begins to occur, was estimated to be 0.015 [see Section 2.2] for particles with 0.5 μm asperities and 100 μm in size. The actual ratio is $b^* < b_c^*$, due to drying limitations, but this does not mean that coalescence will not occur. At the individual particle and droplet level, it was pointed out in Section 2.2 that droplets must be less than 30 μm in size when impacting particles of 100 μm to avoid coalescence. Table 2.4 shows this to be the case, so coating rather than coalescence is favoured by this design. Unfortunately, predictions of the boundary between the granulation and coating, such as this, were not able to be tested within project time frame.

3.2 Gas Entrainment Rate

The entrainment of gas by the inlet gas jet was critical in the design, as this additional gas flow promotes circulation of the particles and provides air for transporting and drying particles as they pass through the draft tube and drying chamber. In section 2.1 the entrainment of gas by an unrestricted gas jets was observed for varying diameter nozzles positioned at the entrance of the draft tube. This data was in close agreement with the predicted gas entrainment values using equation 2.1, however the restriction of the expanding gas jet by the solids in the spouted bed was not taken into consideration. To determine this effect, a series of experiments were carried out to measure the gas flow through the draft tube as a function of solids loadings and nozzle to draft tube clearance.

These experiments were carried out using the 10 mm diameter inlet nozzle with solids loadings of 50, 100 and 200 g of ground limestone, Omyacal 30/200 with an mean particle diameter of 96 to 110 μm. The nozzle to draft tube clearances were varied between 55 to 25 mm, while the inlet air flow was maintained constant at 120 l/min (0.0026 kg/s) The gas flow through the draft tube was measured base on the differential pressure between the inlet of the draft tube and the throat of the venturi shown in Fig. 2.3.

The experiments were carried out by initially loading the apparatus with the required level of solids and raising the inlet nozzle assembly to reduce the separation between the nozzle and draft tube. Once the position was stabilised the differential pressure between the inlet and throat and the solids circulation patten were noted. These results are presented in table 3.2.

The results indicate generally that the gas jet did not expand and hence gas was no entrained while in the jet was in the solid bed region. This is the same conclusion as

drawn in Section 3.1. Comparing the results to the limiting gas flows calculated in table 2.3, it can be seen that the gas flow through the venturi draft tube approached the calculated level for entrainment only when the solid loads were 50 and 100 grams and the nozzle to draft tube clearances were less than 35 and 25 mm respectively. At this point the expansion of the gas jet was free from solid bed restriction and the solids bed was also clear of the draft tube inlet and therefore gas entrainment occurred. The reason they are not quite as high as the predicted values in table 2.3 is likely to be due to turbulent dissipation of the gas expanding from the nozzle to the inlet section of the venturi. However, under these conditions solids were not entrained and no particle circulation occurred. When the nozzle to draft tube clearance was increased solids begin to be entrained and the pressure differential drops sharply until negative pressure differences were recorded.

Table 3.2 Venturi gas entrainment

	Venturi Pressure (P inlet - P throat), Gas Flow		
Nozzle Clearance	50 g loading	100 g loading	200 g loading
25 mm	130.8 Pa, 0.0059 kg/s	111.9 Pa, 0.0055 kg/s	-93.1 Pa*
35 mm	110.7 Pa, 0.0055 kg/s	27.6 Pa, 0.0027 kg/s	-40.2 Pa*
45 mm	50.1 Pa, 0.0038 kg/s	-5.1 Pa*	-24.6 Pa*
55 mm	18.1 Pa, 0.0022 kg/s	-50.4 Pa*	-19.3 Pa*
	Particle Circulation, Description		
Nozzle Clearance	50 g loading	100 g loading	200 g loading
25 mm	no-circulation	no-circulation	pulsed
35 mm	no-circulation	constant	pulsed
45 mm	constant	pulsed	pulsed
55 mm	pulsed	pulsed	pulsed

* negative pressures are shown and hence gas flows cannot be calculated.

The sharp change in conditions can be explained by energy considerations. When no solids are entrained $P_{inlet} > P_{throat}$ due to the wide cross-sectional area at the inlet. However, when there are solids entrained, momentum transfer occurred for which energy losses are associated. These energy losses can be expressed as pressures attributed to drag, friction and suspension of a mass of particles. Effectively the Bernulli equation between the inlet and venture throat can be written as

$$P_D + P_F + P_{sus} + P_{inlet} + \tfrac{1}{2}\rho U^2_{inlet} = P_{throat} + \tfrac{1}{2}\rho U^2_{throat}$$

The result showed that the pressure difference, $P_{inlet} - P_{throat}$, drops rapidly as the clearance increases and solids are entrained. Further increase in separation increased the pressure losses due to P_D, P_F and P_{sus} which quickly result in a negative pressure difference. It is not possible to deconvolute these terms.

The use of the Bernoulli equation here and in section 2.1 to estimate gas flow velocities erroneously uses the assumption of constant density gas. The experimental pressure differences were significantly greater than the 20 Pa initially expected assuming constant cross-sectional velocities. The expansion of the jet, the turbulence in the vicinity of the draft tube inlet and the entrainment of solids, resulted in the pressure differential being difficult to interpret. As a consequence, the pressure differential was discarded as a meaningful number for evaluation of the performance of the modified spouted bed.

Another consideration is the measurement technique. When the particle bed restricts the entrained air flow, the venturi inlet static pressure (Fig. 2.2) is lower than the static pressure in the throat of the venturi. This occurs because the cross sectional area of the flow is less at the nozzle than in the venturi. Thus, the velocity is higher near the nozzle and the pressure is subsequently lower, even though there is a net flow of momentum through the venturi throat.

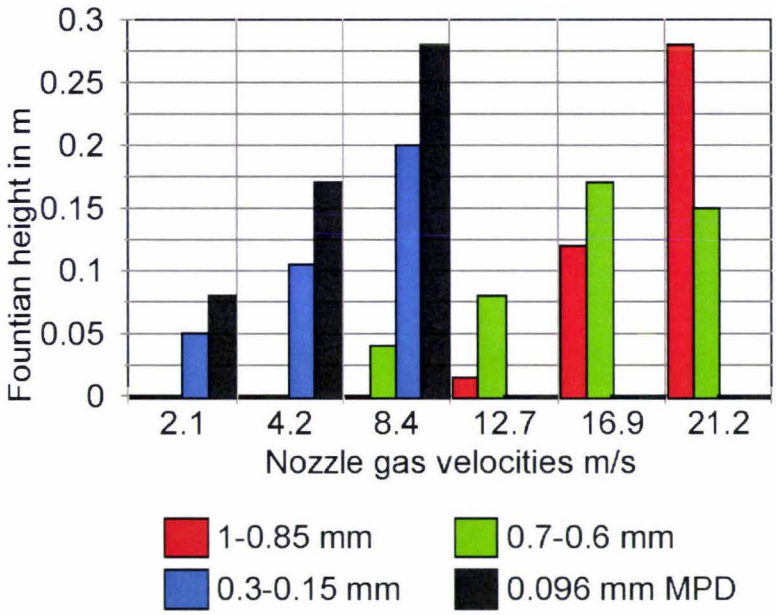

Figure 3.2 Effect of inlet gas velocity and particle size on spouting height for a 40 mm bed depth and a 10 mm nozzle diameter.

Particle circulation was constant when the venturi pressure was in the middle +ve range. For low +ve and for -ve pressures, pulsed flows were observed. Pulsation occurred, firstly, when the solids bed was higher than the draft tube inlet and the nozzle clearance to the draft tube was small. This resulted in the inlet pressure of the draft tube lowering, which induced channelling of gas and solids down through the spouted bed into the draft tube inlet, as these channels increased in size the suction which created then was lost and the channels collapsed, thus establishing an oscillation which is observed as pulsing. Secondly, when the inlet of the draft tube was clear of the bed and the nozzle to draft tube clearance is great the pulsation appears to be due to the spouting gas velocity exceeding a maximum value and the spouted bed transforms into a bubbling/pulsing fluid bed.

A transition from constant to pulsed flow was observed to be related to particle size and inlet gas velocity, as shown in Fig 3.2 where separate experiments were conducted with the venturi draft tube removed. The figure shows the effect of inlet gas velocity and particle size on the fountain height of ground limestone in the modified spouted bed apparatus for a solids bed height of 40 mm. The spouting of limestone less than 0.3 mm in diameter was observed at the lowest levels of gas velocity of 2.1 m/s and was stable until 8.4 m/s, at which point coherent spouting was lost and a bubbling/pulsating fluid bed was formed. However, for particles greater than 0.6 mm in size spouting started initially at higher inlet gas velocities as expected and remained stable up to 21 m/s. This effect may partly explain the observed pulsing effect in the 50 g load trials.

Based on the observed pressure differentials and pulsed flow behaviour, it is concluded that the presence of the draft tube stabilizes the spouting of fine powders by creating a suction effect in the draft tube. Pulsing solids flow will affect the distribution of spray droplets during coating so therefore should be avoided. As was found in the trials shown in table 3.1, neither nozzle diameter or solids loading affects solids circulation time, but table 3.2 shows that nozzle inlet separation distance does affect the solids circulation, at least qualitatively because circulation times were not recorded. Therefore, both the growth rate and microencapsulation experiments described in the next two sections used whatever nozzle separation distance produced constant solids flow.

3.3 Particle Growth Rate Experiments

Investigating particle growth rate, G, requires the large number of variables related to design, operation and the physical properties of binder, solid and gas, to be considered in the design of the experiments. Table 3.3 to 3.6 list all the variables with their description, units and functional dependency. Table 3.3 lists the adjustable variables, that is the variables that can be adjusted within an experiment. To reduce the number of variables some of these are fixed as listed in the right hand column. One binder and one solid particle type are used, along with fixed air flows and temperature conditions. This leaves only operational and selected design variables D_j, Q_b and M_s, the inlet nozzle diameter, the binder flow and the mass of solids in the system respectively.

Table 3.3 Adjustable Variables

Description	Symbol	Units	Function of f{ }	Fixed
binder type			PEG 6000	yes
solid particle type			ground Limestone 96 to 100 micron MPD	yes
inlet nozzle diameter	D_j	m		no
binder concentration in liquid	C_b	kg/kg	0.3 kg/kg	yes
binder mass flow	Q_b	kg/s		no
inlet to draft tube separation	$z_{(nt)}$	m	set at 55 mm	yes
mass of solids	M_s	kg		no
initial solid particle size	D_p	m	{ solid type }	yes
inlet air temperature	T_{gi}	^{o}C	Set at 80 ^{o}C	yes
binder solid softening temperature	T_{sp}	^{o}C	{ binder type} 56 ^{o}C	yes
mass flow of drying air	$Q_{g(dry)}$	kg/s	calib. to pressure reading	yes
mass flow of atomizing air	$Q_{g(atom)}$	kg/s	calib. to pressure reading	yes

Table 3.4 list the parameters which were fixed by the design of the apparatus and cannot be changed in these experiments. Table 3.5 lists the dependant variables and those other variables which affect them.

Table 3.4 Variables fixed by design

Description	Symbol	Units	Function of f{ }	Fixed
area of atomizer air nozzle	A_a	m^2	design	yes
area of atomizer liquid nozzle	A_b	m^2	design	yes
area of filter	A_{filter}	m^2	design	yes
diameter of draft tube inlet	D_1	m	design	yes
diameter of venturi throat	D_2	m	design	yes
% humidity of inlet air	RH_{in}	%		yes
temperature of air supply	$T_{g(supply)}$	^{o}C	assumed to be 20 ^{o}C	yes

Table 3.5 lists the dependent variables that is, variables which are depends upon adjustable variables or upon physical properties. Some of these end up as fixed constants for the range of experiments conducted. This is listed in the right hand column.

Table 3.6 lists the target output variables, that is, those measurable variables that determine the product quality. These are the coated particle size as a function of time which gives the growth rate.

All together, tables 3.3 to 3.6 list 37 variables which may affect the two output variables. However, by fixing the binder and solid type and maintaining constant inlet air flows and temperatures this is reduced to three adjustable variables and eight dependent variables, Table 3.7.

Table 3.5 Dependent Variables				
Description	Symbol	Units	Function of	Fixed
binder droplet size	D_b	m	$Q_{g(atom)}$, Q_b, binder type	yes
porosity of particle bed	ε		ρ_{blk} , ρ_s	yes
% humidity of exhaust	RH_{Exh}	%	$Q_{g(atom)}$, Q_b, $Q_{g(dry)}$,RH_{in}, ρ_g	no
height of solids at inlet of draft tube	h_{bed}	m	M_s, ρ_{blk}	no
mass of single particle	m	kg	ρ_s, D_p	yes
viscosity of air	μ_g	Pa s	T_{syst}	no
viscosity of binder	μ_b	Pa s	T_{sp}, T_{syst}, binder type	yes
number concentration of droplets	N_b	$/m^3$	D_b, ρ_b, $Q_{g(atom)}$, Q_b, $Q_{g(dry)}$	yes
number concentration of solids	N_s	$/m^3$	D_p, ρ_s, $Q_{g(atom)}$, Q_s, $Q_{g(dry)}$	yes
gas entrainment by nozzle/draft tube	$Q_{g(ent)}$	kg/s	RH_{bed}, $z_{(nt)}$, D_{dt} , D_j, θ	no
density of air	ρ_g	kg/m^3	T_{syst}	yes
bulk density of solid particles	ρ_{blk}	kg/m^3	solids particle type	yes
density of solid particle	ρ_s	kg/m^3	solids particle type}	yes
surface asperity of solid particle	h_a	m	solid particle type, time, Q_b	no
binder to solid volume ratio	b*		Q_b, Q_s, ρ_b, ρ_s	no
system temperature	T_{syst}	^{O}C	$Q_{g(atom)}$, $Q_{g(dry)}$, Q_b, RH_{in},RH_{out}, $T_{g(atom)}$, $T_{g(dry)}$	no
gas velocity in draft tube	U_{dt}	m/s	D_{dt}, $Q_{g(atom)}$, $Q_{g(dry)}$, $Q_{g(ent)}$, ρ_g , h_{bed}	no
system pressure	P_{syst}	Pa	A_{filter}, dust loading, $Q_{g(exh)}$	yes
velocity of particles in draft tube	u_{dt}	m/s	coef. drag, g, M_p	yes

Table 3.6 Output Variables				
Description	Symbol	Units	Function of f{ }	Fixed Y/N
mean particle size at time, t	d_p	m	{many.....}	
Particle growth rate	G	m/s	{many.....}	

Table 3.7 Non-Fixed Variables				
Description	Symbol	Units	Function of	Fixed Y/N
inlet nozzle diameter	D_j	m	adjustable variable	no
binder mass flow	Q_b	kg/s	adjustable variable	no
mass of solids	M_s	kg	adjustable variable	no
% relative humidity of exhaust	RH_{Exh}	%	$Q_{g(atom)}$, Q_b, $Q_{g(dry)}$, H_{in}, ρ_g	no
height of solids at inlet of draft tube	h_{bed}	m	M_s, ρ_{blk}	no
viscosity of air	μ_g	Pa s	T_{syst}	no
gas entrainment by nozzle/draft tube	$Q_{g(ent)}$	kg/s	H_{bed}, $z_{(nt)}$, D_{dt}, D_j, θ	no
surface asperity of solid particle	h_a	m	solid particle type, time, Q_b	no
binder to solid volume ratio	b*		Q_b, Q_s, ρ_b, ρ_s	no
system temperature	T_{syst}	^{O}C	$Q_{g(atom)}$, $Q_{g(dry)}$, Q_b, H_{in}, H_{out}, $T_{g(atom)}$, $T_{g(dry)}$	no
gas velocity in draft tube	U_{dt}	m/s	D_{dt}, $Q_{g(atom)}$, $Q_{g(dry)}$, $Q_{g(ent)}$, ρ_g , h_{bed}, solid type	no

A two level factorial design to be developed due to the difficulty in adjusting the inlet gas nozzle diameter as only two nozzles were available, 5 mm and 10 mm. Time constraints also meant no further levels or repetitions were trialed. The mass of solid particles, M_s, is 100 and 300 grams while the binder flow, Q_b will be set at 1 and 4 g/min. From these

operating levels a factorial design was created using the statistical software "MINITAB." This software will be used later to analyse the data and extract the relationships between the experimental variables and the particle growth rate, G. Table 3.8 lists the eight experiments required to complete the experimental analysis of the apparatus with respects to D_j, M_s and Q_b.

Table 3.8 Factorial Design

RunOrder	D_j mm	M_s g	Q_b g/min
1	5	100	4
2	5	100	1
3	5	300	1
4	10	300	4
5	10	300	1
6	10	100	4
7	10	100	1
8	5	300	4

The eight experiments were carried out based on the factorial design with all other adjustable variables maintained constant. The actual experimental conditions are given in table 3.9, which summarizes the operating conditions, measured dependant variables, and the observed particle growth rate, G.

Table 3.9 Experimental operating conditions

Run	Dj mm	Ms g	Binder g/min	Drying l/min	Atomizer Air l/min	Total Inlet l/min
1	5	100	3.87	85.82	29.70	115.51
2	5	100	1.78	98.67	30.53	129.20
3	5	300	1.73	100.96	30.03	130.99
4	10	300	4.11	99.81	30.40	130.21
5	10	300	1.61	100.61	30.91	131.52
6	10	100	4.11	100.58	32.41	132.99
7	10	100	1.64	101.18	27.58	128.76
8	5	300	3.94	104.21	30.35	134.55

Run	Drying Air Temp °C	Air supply Temp °C	System Temp °C	System Air Humidity % RH	G x 10^{-8} m/s	Duration of Run sec
1	101.82	24.32	32.38	72.00	22	1250
2	87.05	23.84	34.51	25.46	2.5	2050
3	92.12	24.12	33.72	25.14	1	3100
4	91.80	23.38	32.98	68.89	16.8	2550
5	94.41	26.25	36.45	22.03	9	3900
6	91.98	23.98	33.58	57.96	13.3	850
7	91.62	25.24	34.78	26.27		0
8	83.63	25.07		59.99	2.5	2345

Solids - Omycal 30/200 ground limestone with a mean particle diameter of between 96 and 100 microns.
Binder - 30% w/w Polyethylene Glycol molecular weight 6000 in water.
Nozzle to inlet separation distance - 55 mm.

The particle growth rate, G, was determined by removing 5 g samples of particles as the particles returned to the spouted bed, using the sample probe built into the viewing chamber above the spouted bed (Fig. 2.1). The samples were then sieved through meshes of, 2.0, 1.0, 0.5, 0.25, 0.125, 0.090 and 0.063 mm. The weights of powder on each sieve and the tray were recorded. The samples were also taken at time intervals which corresponded to the accumulation of binder in the system; for binder flows of 1.69 g/s samples were taken every 600 seconds, and every 250 seconds for the 4.0 g/s binder flow. Figure 3.3. shows the results of the mean particle size analysis as a function of coating time for runs 1, 2, 3, 4, 5, 6 and 8. Unfortunately the conditions for run 7 were not stable and good particle circulation could not be obtained. This was due to poor

entrainment of solids which resulted in the venturi becoming wetted by the blind and blocking.

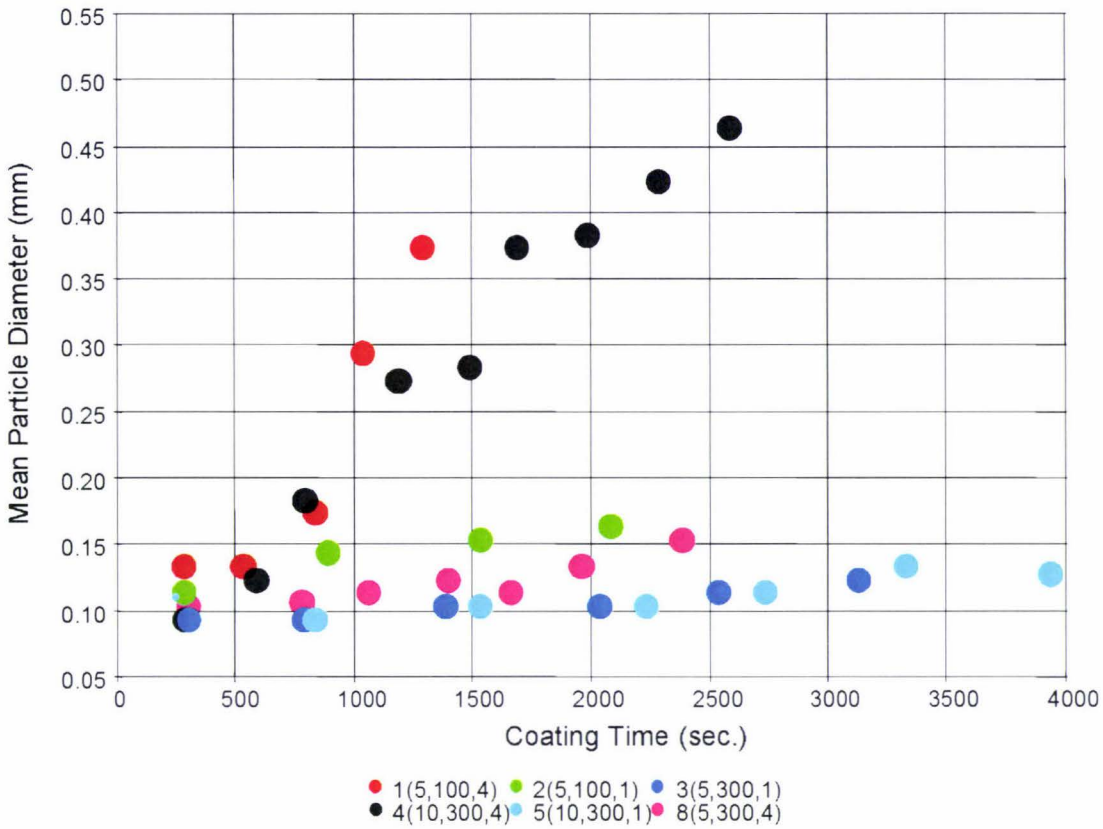

Figure 3.3 Mean particle diameter versus coating time and run number.

The duration of the experimental runs varied for 600 sec to 3900 sec which corresponded to high and low binder flows respectively. The high binder flows induced higher granulation rates and increased the potential for over wetting particles which then become sticky causing the flow of solids into the spouted zone to stop and the particle circulation to collapse.

The growth rate is given in Table 3.10. The expected growth rate can also be calculated assuming all the spray solid end up on the surface of the particles and that the particles do not agglomerate. Table 3.10 shows that the observed particle growth rates are in the order of 10 to 50 time higher than expected, which means that coalescence must be occurring.

Table 3.10 Comparison of experimental particle growth rate and calculated growth rates assuming coating rather than coalescence occurs.

Ms g	Qb g/min	Experimental Particle growth data G ($x10^{-8}$ m/s) D_j = 5 mm	 D_j = 10 mm	G calculated coating only ($x10^{-8}$ m/s)
100	4	22.0	13.3	1.08
300	4	16.8	2.5	0.45
100	1.69	2.5	-----	0.55
300	1.69	1.0	9.0	0.21

To determine the effect of the experimental variables on the particle the growth rate the results were analysed using regression in table 3.11; the absence of run number 7 limits the result to linear effects only. The p-values are all high (> 0.05) indicating that no statistical independence can be established between the variables and no one variable predominantly affects the growth rate.

Table 3.11 Results of statistical analysis

Predicator	Coefficient	P value
Constant	-0.255	0.853
Q_b	3.183	0.317
M_s	-0.02444	0.482
D_j	1.085	0.441

While no statistically significant result was obtained general trends were observed. The increase in nozzle diameter results in an increase in agglomeration when sufficient binder is present as shown by comparing runs 4 and 8. This shows an increase in growth from 2.5 to 16.8 x 10^{-8} m/s with a change in nozzle diameter from 5 to 10 mm. This increase in nozzle diameter decreased the gas jet velocity from 100 to 25 m/s which makes agglomeration more favourable.

Increasing binder flow results in an increase in agglomeration as shown by comparing the growth rates for runs 5 and 4 (9 to 16.8 × 10^{-8} m/s), or runs 3 and 8 (1 to 2.5 × 10^{-8} m/s). In both cases, the system humidity changes from the 20-30% range to

the 60-70% range for a binder flowrate change from 1-4 g/min. This indicates that the drying rate, which is driven by the differential humidity between the wetted particle and the gas flow, is a dominant factor affecting granule growth in the system.

The experimental binder to solids ratio b*, used in these experiments was 5.5×10^{-4} or 1.3×10^{-3} for the two binder addition rates (from tables 3.10 and 3.1 with $\rho_{limestone}$ = 2400 kg/m^3), which was well below 0.002, calculated as the limiting ratio for the drying capacity of the equipment (Section 3.1). At the individual particle and droplet level, even the D_{90} droplet size of 16 μm (table 2.4) impacting a 100 μm spherical limestone particle has a $b^* = 4.1 \times 10^{-3}$, which is significantly below the critical value for coalescence (b_c^* = 0.015, section 2.2, for a hypothetical 100 μm particle with asperity height of 0.5 μm). However, agglomeration did occur, indicating uncontrolled excesses of the critical binder to solids ratio, and/or incomplete drying of wetted product.

3.4 Micro-encapsulation

In addition to granulation, the modified spouted bed can be used for encapsulation, or coating of fine powders. The similarity lies in the application of a liquid binder to the surface of the powder particles, the difference is that in microencapsulation, the wetted particle must be prevented from agglomerating. As discussed in section 1.1 , spouting systems work best on large free flowing particles > 1 mm. The modified spouted bed is designed to coat particles significantly smaller than this by promoting gas and particle recirculation, which allows fine particles to renter the coating zone while maintaining a dilute concentration during the drying stage.

Encapsulation with a polymer coating can alter the dissolution rate of a product which,

for example in oral drugs, can deliver a treatment to a target site based on time and or pH governed by the nature of the coating. The first of these, time dependency, was tested by coating sodium chloride with a semipermeable film, made from Eudragit NE 40D, an aqueous acrylic polymer suspension containing 40% wt of acrylic polymer and clay. The core particle, table salt, was used as an example due to its mean particle diameter being 250 μm and the ease of analysis by column extraction. The dissolution rate of the salt was measured by placing a 0.5 g sample in a column which was extracted by a continous flow of water at 5.0 ml/min. The sodium in the effluent from this column was then continuously measured using a flame photometer. The sodium concentration was then integrated over time to give the % salt in the coated product and the extraction rate. This is further detailed in section 3.4.1

The high viscosity of the polymer NE40 required a glident or pigment to be added to reduce agglomeration. The glidant creates surface asperity which prevents adhesion contact between wetted particle surfaces. For this purpose talc was recommended by the supplier. However, talc must be ball milled into the suspension to produce a colloid. As adequate ball milling was not available to this project, bentonite clay was used as an alternative. As this clay dispersed well by simply mixing with the diluted polymer suspension to give a maximum of 10% additional solids.

Through a number of trials the formulation was defined as 10% Eudragit NE 40D suspension and 10% Bentonite clay in water. This gives a 14% total solids coating agent which is suitable for spraying through the atomizer pump system.

Encapsulation experiments were carried out on 100 gram quantities of table salt using the following operating conditions:

Binder flow	2 g/min
Drying air flow	100 l/min
Atomizer air flow	30 l/min
Drying air temperature	95 ^{0}C
Nozzle to inlet separation distance	55 mm
Inlet nozzle diameter	5 mm

Following coating for 90 minutes, the product was collected and sieved to determine size profile and fractions were analysed for total sodium content and extractions rate.

Measurement of NaCl extraction rate

The extraction rate of Na was measured by placing an accurately weighed sample of between 0.4 and 0.6 grams in a extraction column packed with cotton wool to prevent solids passing. The effluent from this column was then passed through the nebulizer of a EEL flame photometer to measure the sodium content of the effluent with the flow of effluent controlled at 6.3 ml /min. The results of the sodium extraction rate trials are given in figure 3.6 as % of sodium extracted over time.

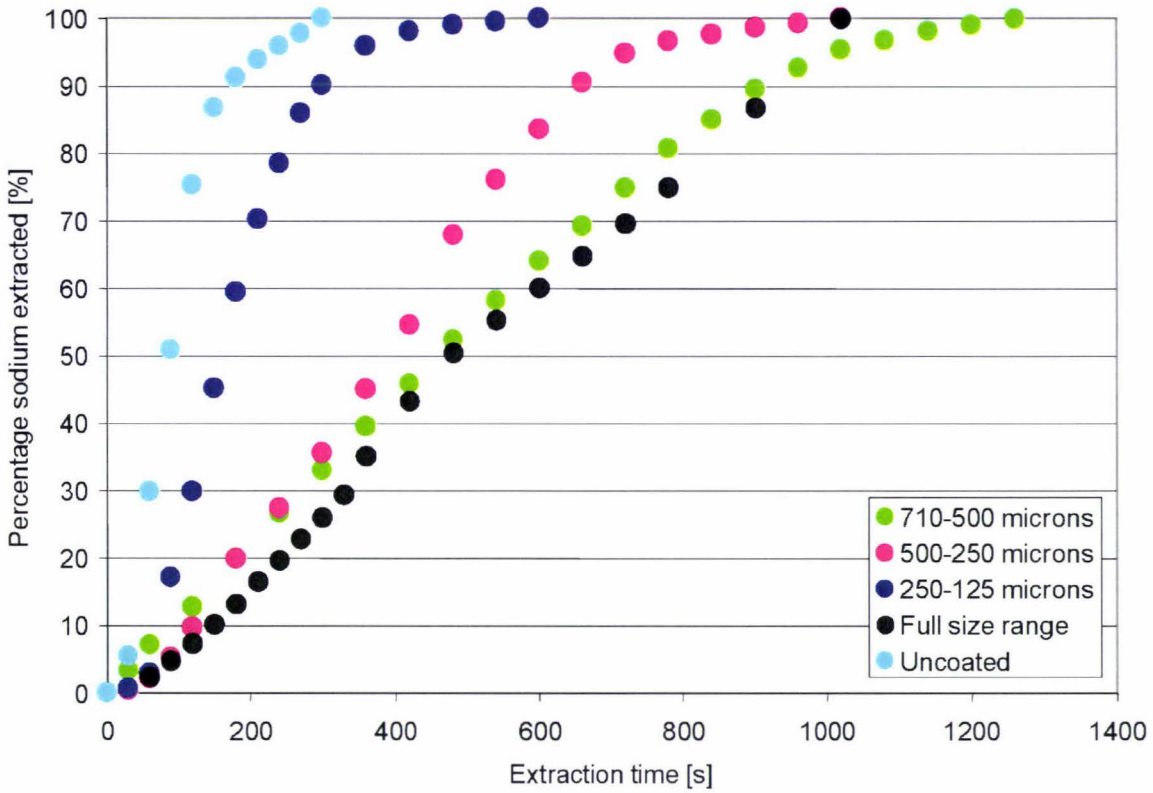

Figure 3.6 Cumulative % sodium extracted over time from coated and uncoated salt.

Table 3.12 and 3.13 give the total sodium chloride content of the extracted samples and the size profile of the final product compared to uncoated salt. Not enough 0-0.125 mm salt was obtained for analysis.

Table 3.12 Sodium chloride content in sieve fractions of coated salt

	0.71-0.5 mm	0.5-0.25 mm	0.25-0.125 mm	Total Sample
% NaCl	91.9	66.4	69.1	80.5

Table 3.13 Size distribution of sample - % mass less than

1.0 mm	0.71 mm	0.5 mm	0.25 mm	0.125 mm
100	96.8	83.4	49	22.2

The analysis of the samples show that the quantity and effectiveness of coating varied with the size range. The effectiveness of encapsulation increases with particle size

meaning that larger particles take longer to dissolve. This result can be related to the film thickness; for example, a spherical particle with an diameter of 0.71 mm with 10% coating by mass has an expected film thickness of 12 μm while a 0.125 mm particle with 10% coating would have a thickness of 3 μm. In fact, the results show that the large particles have 8.1% coating and the small particles have 30.9% coating corresponding to coating thicknesses of 26 and 17 μm respectively. Thus the larger particles have a greater coating thickness and a more effective barrier.

4 Conclusions

The modified spouted bed was designed and constructed in this project to apply a spray of droplets to a powder in a manor which can selectively coat or agglomerate these powder particles. The design utilizes an expanding high velocity gas jet to entrain both gas and solids into a draft tube. This induces re-circulation of fine particles and gas within the apparatus. The performance of the apparatus was assessed in terms of the entrainment of solids and gas, and the operational factors affecting coating and agglomeration. The apparatus was shown to be capable of both coating and agglomerating fine particles.

The particle circulation was measured by using a magnetic particle and inductive pickup coil. The particle mass flow through the spouted zone was found to be 83 to 100 g/s which was independent of solids loadings at 100 and 300 g and independent of the inlet gas nozzle diameter at 5 and 10 mm. This indicates that the gas jet is non-expanding in the solid bed which is consistent with an analysis of the data of Buchanan and Wilson [1965].

Upon exiting the solid bed in the bottom of the apparatus, the gas jet enters the draft tube, the diameter of which contracts into a venturi section. The expansion of the gas jet in the draft tube induces significant suction, observed as a pressure of up to 130 Pa between the inlet of the draft tube and the venturi throat when only gas recirculation occurs. However, when solids are entrained different behaviour is observed. The pressure P_{inlet} - P_{throat} becomes negative, meaning the venturi throat pressure is higher than at the inlet. A number of contributing reasons have been identified, but the most significant is the obstruction caused by solids at the base of the draft tube which reduces

the suction gas flow through the venturi, and hence the suction pressure. Thus, it was found that to maximize the re-circulation of gas and solids, the inlet of the draft tube must be clear of the solid bed.

The model of Ennis [1991] was manipulated to show that for coalescence to occur, particles must be wet and that the critical binder to solid ratio, b_c^*, must be exceeded. Experimentally, coalescence was still observed to occur for binder to solid ratios well below the critical value. The difference between the model and the experimental result is due to insufficient drying of the wetted particles before they return to the solid bed, while the models of Simon *et al.* and Ennis only consider coalescence between individual particles.

Micro-encapsulation was demonstrated in the apparatus by successfully coating fine sodium chloride with a composite acrylic and clay film. The composite formulation was required to overcome the accumulative effect of liquid coating addition, by introducing sufficient glident or pigment, clay in this case, to achieve dry particle surfaces following each successive pass through the spray zone. It was found for the acrylic polymer Eudragit NE 40D, a mixture of 10% polymer and 10% Bentonite clay in water produced little agglomeration in the system. The application of 20 % of this coating mixture on a dry basis to fine sodium chloride crystals of 250 μm in size, achieved a five fold reduction in initial sodium release rates from 0.5 to 0.1 %/s of total sodium content.

The system overall performed well and was shown to be capable of both granulation and coating of particles. The transition from coating to granulation is associated with the liquid film thickness and the binder viscosity and the drying characteristics of the system. This was evident in the change of binder solutions from

Poly-ethylene-glycol to the acrylic polymer Eudragit NE 40D. With the increased viscosity of the Eudragit NE 40D, a glident was required in the formulation to prevent the particles when recirculating to the solid bed at the bottom of the apparatus agglomerating.

References

Brayshaw, D., & Jones, J. R (2000). *Spouted bed granulation of medicated animal feed additives*. Unpublished report, Massey University, Palmerston North, New Zealand.

Buchanan, R. H., & Willson, B. (1965). The fluid-lift solid recirculation. *Journal of Mechanical and Chemical Engineering Translation*, 1, 117.

Dannelly, C. C., & C.R. Leonard, C. R. (1976). Apparatus for Spray Coating of Discrete Particles. US Patent No.04117801.

Ennis, B.J., Tardos, G., & Peffer, R. (1991). A microlevel-based characterization of granulation phenomena. *Powder Technology*, 65, 257-272.

Finch, C.A. (1993). Industrial microencapsulation : Polymers for microcapsule walls. In D. R. Karsa, & R. A. Sthenson (Eds.). Encapsulation and Controlled Release (pp. 1-12).

Ichikawa, H., Tokumitsu, H., Jono, K., Fukuda, T., Osako, Y., & Fukumori, Y. (1994). Coating of pharmaceutical powders by fluidized bed process. VI. *Chemical and Pharmaceutical Bulletin.* 42(6), 1308-1314.

Ichikawa, H., & Fukumori, Y. (1999). Microagglomeration of pulverized pharmaceutical powders using the Wurster process I. *International Journal of Pharmaceutics*, 180, 195-210.

Lain, G., Adams, M. J., & Thornton, C. (1993). A theoretical study of liquid bridge force between two rigid spherical bodies. *Chemical Engineering Science*, 53(19), 3381-3391.

Larson, G. W., & Mallak, P. A. (1963). *Apparatus for coating discrete solid material.* US Patent No. 03110626.

Li, Y. (1998). *Exploration into the nature of insulin binding to oxidized dextran.* Unpublished thesis Massey University, Palmerston North, New Zealand.

Marsters, K. (1976). *Spray drying.* New York: John Wiley and Sons.

Mathur, K. B., & Epstein, N. (1974). *Spouted Beds.* Academic Press, INC. (pp. 6-11).

Perry, R. H.,& Green, D.W (Ed.) (1997). *Perry's chemical engineers' handbook.* McGraw-Hill.

Robins, R. C.,Thomas, J. J., & Cadle, R.D.(1963). Letters to the editor: Aerosol particle encapsulation by simultaneous condensation and polymerization. *Journal of Colloid Science*, 18, 483-488.

Robins, R. C. (1965). *Method of encapsulation of aerosols by in situ polymerisation.* US Patent No. 03219476.

Rynhart, P., & Jones, J. R. (2000) *Micro-encapsulation and Granulation.* Unpublished report, Massey University, New Zealand.

Shelukar, S., Ho, J., & Zega, J. (2000). Identification and characterization of Factors controlling tablet coating uniformity in the Wurster coating process. *Powder Technology*, 110, 29-36.

Simons, S. J. & Fairbrother, R. J. (2000). *Powder Technology*, 110, 44-58.

Simons, S. J ., Seville, J. P., & Adams, M. J. (1994). Analysis of the rupture energy of pendular liquid bridges. *Chemical Engineering Science* 49(14), 2331-2339.

Smith-Johannsen, R., & Wendell, W. M. (1976) *Process of coating particles of less than 20 microns with polymer coating.* US Patent No.03992558.

Tilton, N. (1997). Fluid and particle dynamics : Jet Behavior. In Perry, R. H. (Ed.) (1997) *Perry's Chemical Engineers' Handbook* (pp. 6-20 -6-21). McGraw-Hill.

Wang, S., Xu, J., Wei, J., Shi, G., Bao, X., Bi, H., & Lim, C. (2000). Gas Spouting Hydrodynamics of Fine Particles. *Canadian Journal of Chemical Engineering*, 78, 156-160.

Wurster, D. E., & Lindlof, J. A. (1965). *Apparatus for encapsulation of discrete particles.* US Patent No. US03196827.

Yang, W. C., & Keairns, D. L. (1982). Solids entrainment rate into gas and gas-solid two phase jets in fluidized bed. *Powder Technology*, 33, 89-94.

Zhou, Q., & Chen, X. D. (2000). Lactose hydrolysis of skim milk by immobilized enzyme on cotton cloth. *Proceeding of the 7th Annual New Zealand Engineering and Technology Postgraduates Conference.*

ISBN 0-473-07224-6.